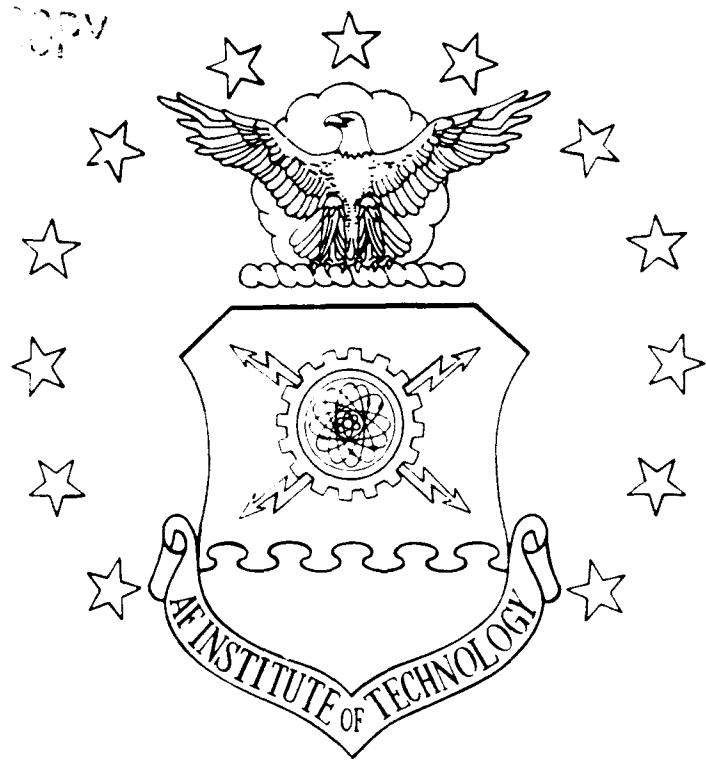


1

AD-A230 576



ANALYSIS OF  
 HYPERSONIC BLUNT-BODY FLOWS  
 USING A  
 TOTAL VARIATION DIMINISHING SCHEME  
 AND THE  
 MACCORMACK SCHEME

THESIS

Montgomery C. Hughson, Captain, USAF

AFIT/CAF/ENV/000-10

W 63 1891

DISTRIBUTION STATEMENT A  
 Approved for public release  
 Distribution Unlimited

DEPARTMENT OF THE AIR FORCE  
 AIR UNIVERSITY  
**AIR FORCE INSTITUTE OF TECHNOLOGY**

Wright-Patterson Air Force Base, Ohio

AFIT/GAE/ENY/90D-10



ANALYSIS OF  
HYPERSONIC BLUNT-BODY FLOWS  
USING A  
TOTAL VARIATION DIMINISHING SCHEME  
AND THE  
MACCORMACK SCHEME

THESIS

Montgomery C. Hughson, Captain, USAF

AFIT/GAE/ENY/90D-10

DTIC  
S  
JAN 08 1991  
D

Approved for public release; distribution unlimited

AFIT/GAE/ENY/90D-10

ANALYSIS OF  
HYPERSONIC BLUNT-BODY FLOWS  
USING A  
TOTAL VARIATION DIMINISHING (TVD) SCHEME  
AND THE  
MACCORMACK SCHEME

THESIS

Presented to the Faculty of the School of Engineering  
of the Air Force Institute of Technology  
Air University

In Partial Fulfillment of the  
Requirements for the Degree of  
Master of Science in Aeronautical Engineering

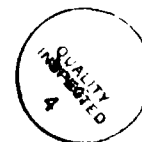
Montgomery C. Hughson, B.S., M.S.

Captain, USAF

December 1990

Accession For	
NTIS GRA&I	J
DTIC TAB	
Unannounced Justification	
By	
Distribution	
Institution	
Dist	Section
A-1	

Approved for public release; distribution unlimited



## Acknowledgments

I dedicate this research to the memory of Capt Wayne Wilsdon. He was a true friend and a kindred spirit on the path to Computational Aerodynamics enlightenment.

I gratefully acknowledge the support and guidance of my advisor, Capt Phil Beran, and of his PhD student, Capt Mark Driver. As Phil put it - "Golf, fishing and CFD, who could ask for anything more?"

I sincerely appreciate the interest and encouragement of Dr Joseph Shang and his fellow researchers of the Wright Research and Development Center. Many useful insights into the physical behavior of fluid dynamics and how to model those phenomena were shared with me. The computer resources were also greatly appreciated.

I also appreciate the advice and support of Lt Cols DeJongh and Hasen. Lt Col Hasen provided a technical paper and the phone number of the author that boosted me over a stumbling block early on.

Finally, as with all of us, I could not have completed the Herculean task of completing this work without the love and support of family and friends. Perhaps the greatest contribution of this work will be a greater appreciation for those who make life's struggles so enjoyable.

Monty

Table of Contents

Acknowledgments . . . . .	ii
List of Figures . . . . .	v
List of Tables . . . . .	vii
List of Symbols . . . . .	viii
Abstract . . . . .	xi
I. Introduction . . . . .	1
1.1 TVD and MacCormack Scheme Background . . . . .	2
1.2 Problem Statement . . . . .	5
II. Analysis . . . . .	5
2.1 Governing Equations . . . . .	6
2.2 Coordinate Transformation . . . . .	8
2.3 Boundary Conditions . . . . .	12
2.3.1. Line of Axisymmetry. . . . .	13
2.3.2. Freestream . . . . .	14
2.3.3. Outflow . . . . .	14
2.3.4. Body Surface. . . . .	15
2.4 Initial Conditions . . . . .	17
2.4.1. Steady-State, Blunt-Body Problem. . . . .	18
2.4.2. Unsteady Shock Impingement Problem. . . . .	20
2.5 Theoretical Predictions . . . . .	21
2.5.1. Shock Standoff Distance . . . . .	21
2.5.2. Modified Newtonian Theory. . . . .	23
2.5.3. Entropy Jump Condition . . . . .	23
2.5.4. Shock Impingement on a Sphere. . . . .	25
2.6 Convergence Criteria . . . . .	28
III. Experimental Data . . . . .	28
IV. Numerical Algorithm Development . . . . .	31
V. Steady-State Solutions of the Euler Equations . . . . .	39
5.1 Computational Grid . . . . .	39
5.2 Shock Standoff Distance and Wave Shape . . . . .	40
5.3 Pressure Distribution . . . . .	49
VI. Dynamic Solutions of the Euler Equations . . . . .	53
6.1 Computational Grid . . . . .	54
6.2 Pressure and Density Flowfield Predictions . . . . .	56
6.3 Comparison of Run Times and Time Step Count . . . . .	71

VII. Conclusions and Recommendations . . . . .	73
7.1 Conclusions . . . . .	73
7.2 Recommendations . . . . .	73
Appendix: Nondimensionalization . . . . .	76
Bibliography . . . . .	78
Vita . . . . .	83

List of Figures

Figure	Page
1. Mapping from Physical to Computational Domain . .	9
2. Body Surface "No-Flow Through" Boundary Condition . . . . .	16
3. Shock Diffraction Process at Two Instances in Time . . . . .	26
4. Double Mach Reflection, Mach = 3.36 . . . . .	27
5. Surface Pressure Distributions, Modified Newtonian Theory and AEDC Data, Mach = 3.0 . . .	30
6. Computational Grid, 51 x 25 . . . . .	40
7. Pressure Along the Line of Axisymmetry, Second- Order TVD and MacCormack Schemes, Mach = 4.03 . .	41
8. Entropy Correction Function Contours, Mach = 3.0 . . . . .	43
9. Pressure Along the Line of Axisymmetry, First- and Second-Order TVD Schemes, Mach = 3.0 . . . .	44
10. Mach Contours, Second-Order TVD Scheme, Mach = 4.03 . . . . .	46
11. Mach Contours, MacCormack Scheme, Mach = 4.03 . .	47
12. Mach Contours, Second-Order TVD Scheme, Mach = 8.1 . . . . .	48
13. Surface Pressure Distribution, First- and Second-Order TVD Schemes, Mach = 3.0 . . . . .	49
14. Surface Pressure Distribution, MacCormack and First-Order TVD Schemes, Mach = 3.0 . . . . .	50
15. Surface Pressure Distribution, MacCormack and Second-Order TVD Schemes, Mach = 4.03 . . . . .	52
16. Computational Grid, 251 x 101 . . . . .	55

17.	Density Contours, Second-Order TVD Scheme, Time = a) .4924, b) .6727, c) .8703 . . . . .	57
17.	Density Contours, Second-Order TVD Scheme, Time = d) 1.0667, e) 1.2708, and f) 1.4765 . . . . .	58
18.	Pressure Contours, Second-Order TVD Scheme, Time = a) .4924, b) .6727, c) .8703 . . . . .	59
18.	Pressure Contours, Second-Order TVD Scheme, Time = d) 1.0667, e) 1.2708, and f) 1.4765 . . . . .	60
19.	Density Contours, MacCormack Scheme, Time = a) .4901, b) .6706, c) .8679 . . . . .	61
19.	Density Contours, MacCormack Scheme, Time = d) 1.0642, e) 1.2690, and f) 1.4747 . . . . .	62
20.	Pressure Contours, MacCormack Scheme, Time = a) .4901, b) .6706, c) .8679 . . . . .	63
20.	Pressure Contours, MacCormack Scheme, Time = d) 1.0642, e) 1.2690, and f) 1.4747 . . . . .	64
21.	Surface Pressure Distribution, Second-Order TVD and MacCormack Schemes . . . . .	67
22.	Density Contours, Second-Order TVD Scheme, Limiter of Eq (46), Time = 1.1546 . . . . .	68
23.	Density Contours, Second-Order TVD Scheme, Time = 1.7510, x = .9990 . . . . .	69
24.	Density Contours, Second-Order TVD Scheme, Time = 2.0527, x = 1.3007 . . . . .	70

List of Tables

Table	Page
1. Shock Standoff Distance, Second-Order TVD Scheme, Theory of Eq (19) and Eq (20), AEDC Experiment . . . . .	44
2. Entropy Jump Condition, Theory of Eq (26), Second-Order TVD and MacCormack Schemes . . . . .	53
3. Comparison of Time Step Count and Time, Second-Order TVD and MacCormack Scheme, Mach = 2.89 . . . . .	72

### List of Symbols

Symbol	Definition
$a$	eigenvalue
$A$	flux Jacobian for x direction
$B$	flux Jacobian for y direction
$c$	speed of sound
$c_p$	specific heat at constant pressure
$c_v$	specific heat at constant volume
$D$	density of Roe averaging
$e$	internal energy per unit mass
$E$	flux vector in x direction
$\hat{E}$	numerical flux in $\xi$ direction
$E_t$	total energy per unit volume
$F$	flux vector in y direction
$\hat{F}$	numerical flux in $\eta$ direction
$g$	limiter function
$H$	total enthalpy
$i$	$\xi$ index
$I$	maximum $\xi$ index
$j$	$\eta$ index
$J$	maximum $\eta$ index
$\hat{J}$	Jacobian of the transformation
$k_h, k_{h1}, k_{h2}$	constants based on metrics
$L$	time-splitting operator

$L_2$	Euclidean norm
$m_x, m_y$	x and y momentum
$M_\infty$	freestream Mach number
$p$	pressure
$R$	eigenvector, Riemann invariant
$R$	gas constant
$s$	entropy
$S$	source term
$S$	sign function
$t$	time
$T$	temperature
$u$	x component of velocity
$U$	vector of dependent variables
$u_c, U_c, v_c$	contravariant velocity
$v$	y component of velocity
$\alpha$	difference of the characteristic variables
$\gamma$	ratio of specific heats
$\delta_o$	shock standoff distance
$\delta_f$	entropy correction function
$\delta_p$	entropy correction parameter
$\epsilon$	density ratio
$\eta$	transformed coordinate
$\theta, \Theta$	angular measure
$\xi$	transformed coordinate

$\rho$	density
$\sigma$	<u>effective</u> numerical viscosity coefficient
$\psi$	numerical viscosity coefficient

#### Subscript Definition

$B$	body
$c$	contravariant
$f$	function
$i$	$\xi$ index
$j$	$\eta$ index
$MAX$	maximum value
$n$	normal, normal derivative
$o$	standoff
$p$	parameter, pressure
$S$	shock
$Stag$	stagnation quantity
$t$	total, tangential
$x$	differentiation with respect to $x$ direction
$y$	differentiation with respect to $y$ direction
$\eta$	differentiation with respect to $\eta$ direction
$\xi$	differentiation with respect to $\xi$ direction
$\infty$	condition at infinity

## Superscript Definition

$h$	time step
$l$	vector component
$n$	time level
$\hat{z}$	denotes quantity transformed to computational domain
$*$	dummy time index, nondimensional quantity
$\beta$	0: two-dimensional, 1: axisymmetric
$1, 2, 3, 4$	vector component

## Abstract

An explicit, second-order accurate, total variation diminishing (TVD) scheme and the MacCormack scheme are applied to the Euler equations in axisymmetric form to study hypersonic blunt-body flows. The modified-flux approach of Harten, with modification by Yee<sup>1</sup>, for two-dimensional flows is extended to treat axisymmetric flows. Calculated flow properties for the steady-state, blunt-body problem such as shock standoff distance, bow-shock shape, surface pressure distribution and entropy jump conditions are compared to theory, results of the MacCormack scheme, and experimental data for Mach numbers of 3.0, 4.03, 5.06, 6.03 and 8.1. Additionally, the TVD and MacCormack schemes are used to simulate numerically the unsteady shock impingement on a sphere. Results are compared to experimental data for a shock Mach number of 2.89. Analysis of the numerical simulations provide suitable ranges of values for the entropy correction parameter and the Courant (CFL) number. A brief comparison of limiters for the unsteady problem is also presented. The high-resolution, shock-capturing capability and robustness of the TVD scheme is clearly shown.

ANALYSIS OF HYPERSONIC BLUNT-BODY FLOWS  
USING A  
TOTAL VARIATION DIMINISHING (TVD) SCHEME  
AND THE  
MACCORMACK SCHEME

I. Introduction

Programs of national significance such as the National Aerospace Plane (NASP), the Strategic Defense Initiative (SDI) and the Aeroassisted Orbital Transfer Vehicle (AOTV) have renewed interest in hypersonic aerodynamics. Hypersonic wind tunnels and ground-test facilities developed in the 1960's during the initial era of hypersonics research interest fell into disuse following the drastic funding cuts of the 1970's and are just now being rebuilt and refurbished<sup>2</sup>. Due to these constraints on physical testing of hypersonic vehicle models, numerical simulations become particularly important. Computational fluid dynamics (CFD) offers immediate means for hypersonic aerodynamics research, development and design for a number of reasons. There are three main advantages of CFD over field tests and laboratory experiments<sup>3</sup>:

- 1) lower cost,
- 2) increased data collection capability - virtually any flow quantity can be computed in the field of interest, and
- 3) exact repeatability, precise control over initial and boundary conditions, and the related capability to independently vary important parameters.

Blunt-body flows are of particular interest because hypersonic vehicles are designed with blunt noses to reduce aerodynamic heating. The solution of the Euler equations of fluid flow in the nose region of a blunt-body, such as those presented in this study, provide numerical estimates of shock standoff distance, bow-shock shape, and surface pressure distributions. Additionally, these solutions provide edge properties for input to boundary layer codes, which in turn can provide estimates of heat transfer and skin friction. In the study of transient flow phenomena, application of the numerical schemes to the unsteady shock impingement problem can provide pressure and density contours about a sphere as a blast-wave passes over it. This ability to accurately simulate the complex shock-diffraction process is particularly important for the analysis of a building's ability to maintain structural integrity during the passage of a blast-wave from a nuclear explosion.

### 1.1 TVD and MacCormack Scheme Background

In this section, the background information is condensed from the excellent survey reported by Yee in Reference 1.

For complex flowfields, monotone and first-order upwind schemes are too diffusive. Monotone schemes produce smooth transitions near discontinuities, but they are only first-order accurate. High-resolution shock-capturing numerical simulations are not possible with these schemes on grids of

reasonable size. Schemes of higher-order accuracy have been developed over the past decade and the development of such is an area of active research.

Classical shock-capturing schemes use linear numerical dissipation - the same amount everywhere or consists of adjustable parameters for each problem. Modern schemes employ numerical dissipation in a nonlinear fashion - the amount varies from grid point to grid point and is implemented automatically within the scheme with few, if any, adjustable parameters<sup>1</sup>. This technique was developed to overcome the following deficiencies:

- 1) development of spurious oscillations whenever the solution is not smooth,
- 2) development of nonlinear instabilities when discontinuities are encountered, and
- 3) the selection of a nonphysical solution.

Total variation diminishing (TVD) schemes are a class of modern, high-resolution, shock-capturing schemes introduced by Harten<sup>4</sup>. A main objective of this class of schemes is to ensure that solutions of the Euler equations converge to physically correct solutions. This is extremely important if one is dealing with fluid flows for which analytic solutions or experimental data are not readily available. The basic idea behind the notion of a TVD property is that the total variation of the numerical solution of an initial-value problem will not grow as the solution evolves in a time-like fashion. See Reference 4 for precise mathematical details.

It should be emphasized that the TVD property is only valid for systems of homogeneous scalar hyperbolic equations. For nonhomogeneous hyperbolic equations, in order for the source term to not influence the TVD property, it is restricted to a special class of functions and fluid flows<sup>1</sup>. For finite-volume, upwind TVD schemes, similar to the one employed in this study, Wang and Widhopf<sup>5</sup> prove the TVD property is satisfied for the axisymmetric version of the Euler equations written in conservation form.

The MacCormack scheme has been an industry standard for many years and details of the numerical algorithm other than boundary conditions are not reported in this study. The scheme has been applied to a wide variety of fluid flow problems. Application of the scheme to the Navier-Stokes equations for axisymmetric flows with finite-rate chemical kinetics has been reported by Shang and Josyula<sup>6</sup>. The MacCormack scheme applied to the Euler equations in axisymmetric form was used for this study.

As will be shown in the sections forthcoming, comparisons between flowfield properties computed with the TVD scheme and the MacCormack scheme are very good. Comparisons between the schemes, theory, and experiment are also very good.

## 1.2 Problem Statement

The main objectives of this study are to show the high-resolution and robustness capabilities of the two-dimensional TVD scheme extended to axisymmetric form. Applications to the steady-state, blunt-body problem and the problem of unsteady shock impingement on a sphere provide a wide range of flowfield features possible with the Euler equations. Furthermore, within the context of each application, suitable values of parameters inherent to using the scheme, such as Courant (CFL) number, entropy correction parameter,  $\delta_p$ , appropriate limiters as well as boundary and initial conditions, are numerically investigated.

For the steady-state, blunt-body problem, flowfield quantities computed with the TVD scheme will be compared to theory, experimental data, and results of the MacCormack scheme. Specific items considered are the shock standoff distance, bow-shock shape, body surface pressure distribution, and the entropy jump condition.

For the unsteady impingement of a shock on a sphere, flowfield quantities computed with the TVD scheme will be compared to theory and experimental data. Specific items considered are the density and pressure distributions in the flowfield and the resolution of the complex interactions.

## II. Analysis

A discussion of the governing equations, the transformation from the physical domain to the computational domain, boundary conditions, initial conditions, theoretical predictions, and a description of the convergence criteria will be presented in the next few sections.

### 2.1 Governing Equations

The Euler equations are statements of conservation of mass, momentum and energy. These principles are<sup>7</sup>:

- 1) mass can be neither created nor destroyed,
- 2) the time rate of change of momentum of a body equals the net force exerted on it, and
- 3) energy can be neither created nor destroyed; it can only change in form.

The properties of the fluid medium are characterized by density  $\rho$ , the pressure  $p$ , the internal energy per unit mass  $e$ , and the fluid velocity  $\underline{u}$  as functions of position and time. An equation of state is assumed of the form  $e = f(p, \rho)$ . Additionally, it is assumed that no viscous forces, body forces, heat conduction or energy sources are present. The conservation form of the two-dimensional Euler equations can be given in conservative variables  $\rho$ ,  $\rho u$ ,  $\rho v$ , and  $E_t$ . The equations have the ability to describe internal discontinuities such as shock waves (where  $\rho$ ,  $\rho u$ ,  $\rho v$ , and  $e$  are discontinuous) and contact surfaces (where  $\rho$ , and  $e$  are discontinuous) which are

frequently encountered in fluid flow<sup>8,9</sup>. The Euler equations can be written in flux vector form:

$$\frac{\partial U}{\partial t} + \frac{\partial E(U)}{\partial x} + \frac{\partial F(U)}{\partial y} = S \quad (1)$$

where

$$U = \begin{bmatrix} \rho y^\beta \\ m_x y^\beta \\ m_y y^\beta \\ E_t y^\beta \end{bmatrix} \quad E = \begin{bmatrix} m_x y^\beta \\ (p + m_x^2/\rho) y^\beta \\ m_x v y^\beta \\ m_x/\rho (E_t + p) y^\beta \end{bmatrix}$$

$$F = \begin{bmatrix} m_y y^\beta \\ m_y u y^\beta \\ (p + m_y/\rho) y^\beta \\ m_y/\rho (E_t + p) y^\beta \end{bmatrix} \quad S = \begin{bmatrix} 0 \\ 0 \\ \beta p \\ 0 \end{bmatrix} \quad (2)$$

and  $\beta = 0,1$  for two-dimensional and axisymmetric cases, respectively;  $m_x = \rho u$ ,  $m_y = \rho v$ , the total energy,  $E_t$ , is

$$E_t = \rho e + \frac{m_x^2 + m_y^2}{2\rho} \quad (3)$$

and pressure is given as

$$p = (\gamma - 1) \rho e \quad (4)$$

## 2.2 Coordinate Transformation

For the numerical solution of these partial differential equations (PDEs), it is imperative that boundary conditions be accurately represented. In fact, the boundary conditions are what differentiate one fluid flow problem from another, as far as the governing equations are concerned<sup>10</sup>. In general, the Cartesian coordinate system is limited in usefulness to configurations that can be represented by a rectilinear shape. For a more general body shape, a transformation of the governing equations to a curvilinear, boundary-conforming system is more appropriate. A transformation of the form  $\xi = \xi(x, y)$  and  $\eta = \eta(x, y)$  is used to map Eq (1) from a general physical domain  $(x, y)$  to a rectangular computational domain  $(\xi, \eta)$  as illustrated in Figure 1. The transformed strong conservation form of the Euler equations, assuming the computational grid is fixed in time, is

$$\frac{\partial \hat{U}}{\partial t} + \frac{\partial \hat{E}(\hat{U})}{\partial x} + \frac{\partial \hat{F}(\hat{U})}{\partial y} = \hat{S} \quad (5)$$

where

$$\begin{aligned} \hat{U} &= \hat{J}U \\ \hat{E} &= \hat{J}(\xi_x E + \xi_y F) \\ \hat{F} &= \hat{J}(\eta_x E + \eta_y F) \\ \hat{S} &= \hat{J}S \end{aligned} \quad (6)$$

and  $\hat{J} = x_\xi y_\eta - x_\eta y_\xi$  is the Jacobian of the transformation. The

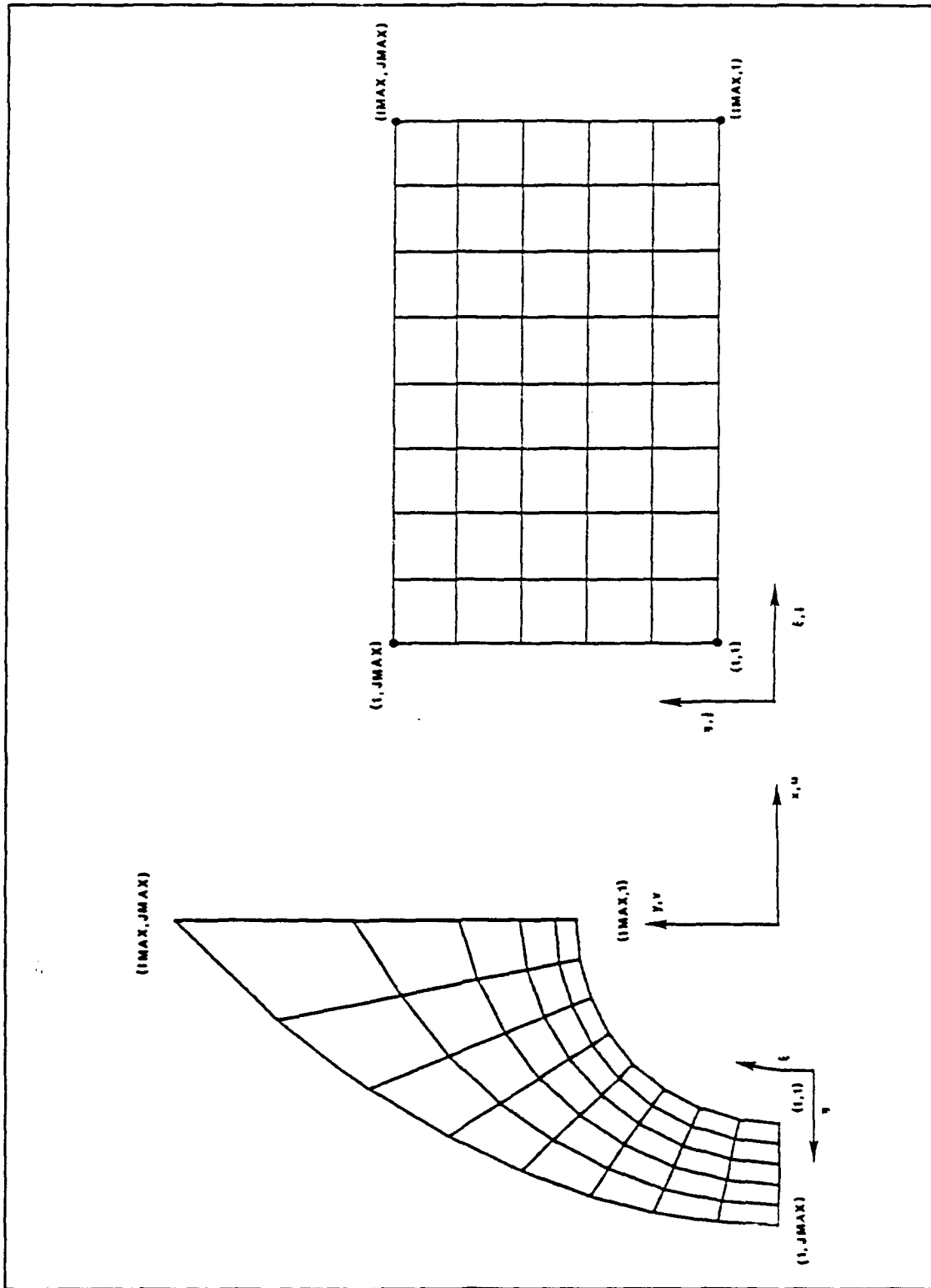


Figure 1. Mapping from Physical to Computational Domain

solution via Roe's approximate Riemann solver<sup>11</sup> (sometimes referred to as the "local characteristic approach") requires evaluation of the Jacobians  $\hat{A}$  and  $\hat{B}$  of  $\hat{E}$  and  $\hat{F}$ . Through the application of the chain rule these can be written as

$$\begin{aligned}\hat{A} &= (\xi_x A + \xi_y B) \\ \hat{B} &= (\eta_x A + \eta_y B)\end{aligned}\quad (7)$$

where  $A = \partial E / \partial U$  and  $B = \partial F / \partial U$ . The eigenvalues of  $\hat{A}$  and  $\hat{B}$  are

$$a_h = \begin{pmatrix} h_x u + h_y v - k_h c \\ h_x u + h_y v \\ h_x u + h_y v + k_h c \\ h_x u + h_y v \end{pmatrix}\quad (8)$$

where

$$\begin{aligned}h &= \xi \text{ for } \hat{A} \\ h &= \eta \text{ for } \hat{B}\end{aligned}\quad (9)$$

and

$$\begin{aligned}h_x u + h_y v &= U_c \\ c &= \sqrt{\gamma P / \rho} \\ k_h &= \sqrt{h_x^2 + h_y^2}\end{aligned}\quad (10)$$

where  $U_c$  is referred to as the contravariant velocity. The contravariant base vectors of the curvilinear coordinate system are normal to the coordinate surfaces<sup>12</sup>, and the contravariant velocities are the inner product of the base vectors with the velocity vector.

The right eigenvectors of  $\hat{A}$  and  $\hat{B}$ ,  $(R_h^1, R_h^2, R_h^3, R_h^4)$ , are

$$\begin{aligned}
 R_h^1 &= \begin{bmatrix} 1.0 \\ u - k_{h1}C \\ v - k_{h2}C \\ H - k_{h1}uC - k_{h2}vC \end{bmatrix} & R_h^2 &= \begin{bmatrix} 1.0 \\ u \\ v \\ \frac{1}{2}(u^2 + v^2) \end{bmatrix} \\
 R_h^3 &= \begin{bmatrix} 1.0 \\ u + k_{h1}C \\ v + k_{h2}C \\ H + k_{h1}uC + k_{h2}vC \end{bmatrix} & R_h^4 &= \begin{bmatrix} 0.0 \\ -k_{h2} \\ k_{h1} \\ k_{h1}v - k_{h2}u \end{bmatrix} \quad (11)
 \end{aligned}$$

where

$$\begin{aligned}
 H &= \frac{\gamma P}{(\gamma-1)\rho} + \frac{1}{2}(u^2 + v^2) \\
 k_{h1} &= \frac{h_x}{\sqrt{h_x^2 + h_y^2}} = \frac{h_x}{k_h} \\
 k_{h2} &= \frac{h_y}{\sqrt{h_x^2 + h_y^2}} = \frac{h_y}{k_h}
 \end{aligned} \quad (12)$$

Furthermore, the total enthalpy and the speed of sound can be written in terms of the conserved variables as

$$\begin{aligned}
 H &= (E_t + \frac{P}{\rho}) \\
 P &= (\gamma-1)(E_t - (m_x^2 + m_y^2)/(2\rho)) \\
 C^2 &= (\gamma-1)(H - (m_x^2 + m_y^2)/(2\rho^2))
 \end{aligned} \quad (13)$$

For the actual implementation of the equations, the flow quantities were nondimensionalized in a consistent fashion as shown in the Appendix.

### 2.3 Boundary Conditions

The finite-volume TVD scheme constructs cells using node points as vertices in the physical domain. The ensuing grid of cell centers is then used for actual calculations. Furthermore, mirror images (referred to as ghost points in this study, sometimes also referred to as phantom points) are placed at cell centers just outside the physical domain to aid in the enforcement of the boundary conditions. The finite-difference MacCormack scheme, however, uses actual node points for calculations and does not use ghost points.

A general mapping of the physical domain to the computational domain was illustrated in Figure 1. The physical domain shown was that for the steady-state calculations whereby a blunt-body with a spherical nose is modelled. Referring to Figure 1, the physical domain consists of:

- 1) a line of axisymmetry (front stagnation line),
- 2) a parabolic outer boundary where freestream conditions are imposed,
- 3) a supersonic/hypersonic outflow boundary, and
- 4) the spherical body surface.

The parabolic shape of the outer boundary was selected based on the fact that bow-shock shapes are parabolic. The intent was to minimize the number of grid points between the freestream boundary and the captured shock.

For the unsteady calculations, the physical domain is a half-circle (sphere) as will be shown in Section VI. The physical domain consists of:

- 1) front and
- 2) rear lines of axisymmetry (stagnation lines),
- 3) a circular outer boundary where freestream conditions are imposed, and
- 4) the spherical body surface.

The boundary conditions are described in detail in the next few sections.

2.3.1. Line of Axisymmetry. For the TVD scheme, the reflection principle was applied across the line of axisymmetry. Derivatives of conserved variables normal to the line of axisymmetry and the  $v$  component of velocity were specified to vanish. Furthermore, since the physical area on the line of axisymmetry is zero, the flux at that cell interface was also set to zero. Exactly how this is implemented in the numerical algorithm will be shown in Section IV. For the MacCormack scheme, a limiting form of the governing axisymmetric equations, developed by Shang and Josyula<sup>6</sup>, was used to overcome the geometric singularity at the line of axisymmetry encountered in the finite-difference formulation. As will be shown in the steady-state solutions of the Euler equations in Section V, oscillations of flowfield quantities in the stagnation region near the line of axisymmetry are a common occurrence. In some cases, these oscillations lead to numerical instabilities.

2.3.2. Freestream. It is assumed that the parabolic outer boundary for the steady-state, blunt-body problem, and the circular outer boundary for the unsteady shock impingement problem, are located sufficiently far away from the body surface that freestream boundary conditions can be imposed. For the unsteady calculations, it was necessary to track the planar moving shock wave and impose pre- and post-shock boundary conditions consistent with the Rankine-Hugoniot relations for changes across a normal shock.

2.3.3. Outflow. The outflow boundary condition described in this section pertains to the steady-state, blunt-body problem shown in Figure 1. At the top of the sphere, the fluid flow has accelerated to a supersonic Mach number from a subsonic Mach number in the nose region immediately behind the normal shock. Two-point extrapolation was used for the outflow boundary values in the TVD scheme. A "no-change" or one-point extrapolation method worked just as well and was used in the MacCormack scheme. One advantage of two-point extrapolation is that contours of flowfield values are smoother at the outflow boundary for relatively coarse grids. This will be apparent in the Mach contour plots to be shown in Section V.

2.3.4. Body Surface. The following paragraph is quoted directly from Anderson et al<sup>8</sup>:

We now address the problem of applying surface boundary conditions when shock-capturing methods are used. As Moretti (1969) has pointed out, the correct application of boundary conditions is a difficult task. Incorrect wall conditions can provide locally polluted results and in many cases can destroy a solution. Hyperbolic equations are particularly sensitive. Due to their wave-like nature, boundary errors are propagated throughout the mesh reflecting until actual instability can result.

For these reasons, particular care was taken when selecting the following body surface boundary conditions.

At the sphere surface, a "no-flow through" condition was imposed. That is, the normal component of velocity is set to zero while the tangential component is preserved. For the TVD scheme, ghost points inside the physical body surface were used and these conditions are

$$\begin{aligned} u_{n1} &= -u_{n2} \\ u_{t1} &= u_{t2} \end{aligned} \quad (14)$$

where  $j = 1$  corresponds to the  $\eta$  coordinate in the radial direction for the ghost point as shown in Figure 2. The velocity values at the ghost point are determined by

$$\begin{bmatrix} u_1 \\ v_1 \end{bmatrix} = \begin{bmatrix} -\cos^2\theta + \sin^2\theta & -2\cos\theta\sin\theta \\ -2\cos\theta\sin\theta & -\sin^2\theta + \cos^2\theta \end{bmatrix} \begin{bmatrix} u_2 \\ v_2 \end{bmatrix} \quad (15)$$

For the MacCormack scheme, the normal component of velocity at the node point on the surface is set to zero and the

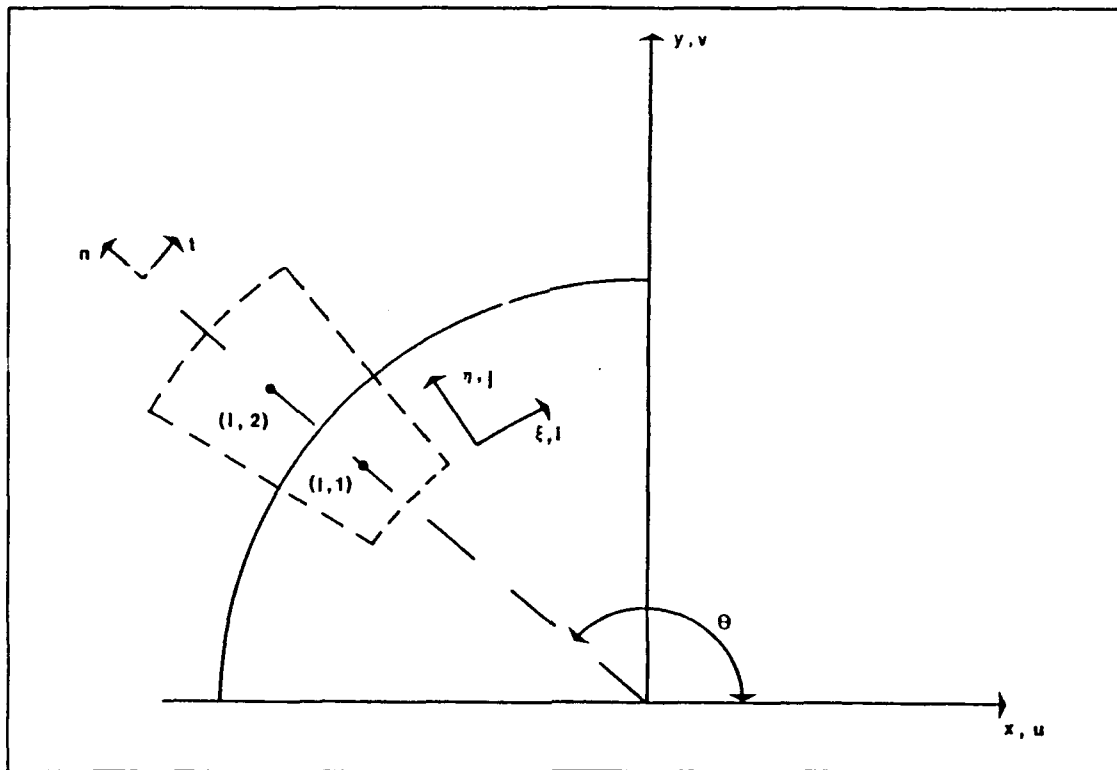


Figure 2. Body Surface "No-Flow Through" Boundary Condition

tangential component is set equal to the value at the first node point off the surface.

To obtain the pressure at the body surface, the normal momentum equation is used as recommended by Pulliam and Steger<sup>13</sup>:

$$\begin{aligned}
 -\rho U_c (\eta_x u_\xi + \eta_y v_\xi) &= (\eta_x \xi_x + \xi_y \eta_y) p_\xi + (\eta_x^2 + \eta_y^2) p_\eta \\
 &= p_n \sqrt{\eta_x^2 + \eta_y^2}
 \end{aligned}
 \tag{16}$$

where  $p_n$  is the pressure normal to the body surface. Second-

order accurate central-differencing is used for both  $\xi$  and  $\eta$  direction derivatives and  $U_c$ , the contravariant velocity, is given by

$$U_c = \xi_x u + \xi_y v \quad (17)$$

An adiabatic wall condition and the equation of state are used to calculate the density. Even though the specification of the temperature gradient at the body surface is inconsistent with the Euler equations, Pulliam and Steger<sup>13</sup> report that it has been used by others with no apparent degradation of the solution. A recent paper by Driver and Beran<sup>14</sup>, using a TVD scheme similar to the one developed in this study, used this same boundary condition for the blade surface in a high-work, low aspect ratio turbine flow numerical simulation. Their surface results were all well within a few percent of experimental data. These results would seem to justify the use of this particular boundary condition. The total energy,  $E_c$ , is calculated from the surface values of density, pressure, and velocity.

For the TVD scheme, the normal momentum equation is applied at the first cell center off the body surface to obtain values at the ghost point. For the MacCormack scheme, the equation is applied at the first node point off the surface to obtain values at the surface.

A reflection method was also investigated for the TVD scheme whereby density and total energy at the ghost points

were set equal to the values at the first cell center off the body surface. This technique slightly overpredicted pressure at the surface compared to pressure predicted by the application of the normal momentum equation. Furthermore, Roache<sup>15</sup> has shown that the reflection method is an inconsistent boundary condition for a curved surface and should only be used for flat surfaces. Anderson et al<sup>8</sup> also stipulate that the reflection boundary condition "is very inaccurate on bodies in regions with high curvature."

#### 2.4 Initial Conditions

Many numerical schemes are extremely sensitive to initial conditions and their effects on the transient or state-state solution is an area of ongoing research. Care must be taken to apply reasonable, physically realistic initial conditions to start calculations<sup>16</sup>. For these reasons, detailed discussions of the initial conditions for the steady-state and the unsteady computations will be presented in the following sections.

2.4.1. Steady-State, Blunt-Body Problem. For numerical computations of the blunt-body problem in hypersonic flows, many numerical procedures use theory to predict the shock standoff distance and bow-shock shape, and then apply the Rankine-Hugoniot relations and modified Newtonian theory to provide a smooth initial state of flowfield quantities. In

this study, a first-order TVD scheme was employed to establish an initial condition for the second-order TVD and MacCormack schemes for a number of reasons. First of all, as part of the evolutionary development of the second-order TVD scheme, a first-order TVD scheme was constructed. It was a simple procedure to incorporate that solution as an initial state for the second-order schemes. Secondly, that initial state contained a discontinuity in pressure at the stagnation point and an unsmooth flowfield as seen in the Mach contour values (which will be shown in Section V). This provided a good test of the robustness of the second-order TVD and MacCormack schemes. Finally, theoretical solutions for an initial state of a general hypersonic blunt-body problem may not always be readily available to a design engineer. The first-order TVD scheme is very robust and can provide a rough prediction of a blunt-body flowfield. Of course, any numerical solution should be compared to related theoretical predictions to ensure that qualitative features are correctly modelled.

Within the first-order TVD scheme, the flowfield is initialized to freestream conditions throughout and then run for 500 iterations (time steps) with a CFL number of 0.9. This technique is sometimes referred to as an impulsive start. Peyret and Taylor<sup>16</sup> report that Grossman and Moretti found that an impulsive start tended to make transonic calculations unstable while a gradual or ramped start worked reasonably

well. This technique has also been employed in Program EAGLE<sup>17</sup> for transonic calculations in the form of gradual application of the "no-flow through" body surface boundary condition. For the supersonic/hypersonic numerical simulations in this study, the impulsive start of the first-order TVD scheme was very stable. The impulsive start procedure allowed a rough development of the salient flow features - such as shock standoff distance and bow-shock shape - to take place. As mentioned above, this solution constituted the initial state used by the second-order TVD and MacCormack schemes. The second-order TVD scheme was normally run for 500 to 1000 iterations with a CFL number of 0.5 before the convergence criteria, to be discussed in the next section, were satisfied. For the MacCormack scheme, at Mach numbers greater than 3.0, it was necessary for stability to keep the CFL number at or below 0.1. In addition, the smoothing coefficients for the MacCormack scheme were set to 4.0. Comparison plots of the initial state from the first-order TVD scheme and final converged solutions from the second-order TVD and MacCormack schemes will be presented in Section V.

2.4.2. Unsteady Shock Impingement Problem. For the numerical simulation of the unsteady shock impingement on a sphere, an initial shock location was assumed at  $x = -0.75$  for the Mach 2.89 case. Flowfield values are initialized to pre- and post-shock conditions and the unsteady solutions are

impulsively started from that state. Because the dynamic process of the shock striking and passing over and beyond the sphere occurs on the order of milliseconds, the incident shock wave can be approximated with good accuracy by a normal shock wave<sup>18</sup>. As mentioned in Section 2.3.2, it was also necessary to track the shock along the outer boundary and impose pre- and post-shock conditions there as the shock propagated in time.

## 2.5 Theoretical Predictions

To ensure that the numerical simulations accurately model the qualitative features of the steady-state, blunt-body problem and the problem of unsteady shock impingement, comparisons will be made to theoretical predictions in the results sections. The next few sections present the theory.

2.5.1. Shock Standoff Distance. The inviscid flowfield in the stagnation region between the shock and the body surface for steady, axisymmetric flow about a blunt-body at hypersonic Mach numbers is governed by the hypersonic boundary layer equations. Furthermore, in the stagnation region, the detached bow-shock wave is nearly normal and hence, the Mach number is subsonic and the flow is considered incompressible. Shock standoff distance formulas are derived as functions of the density ratio and the radius of the shock. The Rankine-Hugoniot relation for the density ratio  $\epsilon = \rho_w/\rho_s$  across the

normal shock, in the limiting case of infinite Mach number and for a value of the ratio of specific heats,  $\gamma = 1.4$ , becomes

$$\epsilon = \frac{\gamma-1}{\gamma+1} = 0.167 \quad (18)$$

As reported by Reshotko<sup>19</sup>, Hayes derives the shock standoff distance,  $\delta_o$ , under these assumptions as

$$\frac{\delta_o}{R_s} \approx \frac{\epsilon}{1 + \sqrt{2\epsilon}} \quad (19)$$

where  $R_s$  = radius of the shock. Additionally, Truitt<sup>20</sup> derives the following formula for axisymmetric blunt-body flow:

$$\frac{\delta_o}{R_s} \approx \epsilon \left| \frac{-1 + \sqrt{1 - (1-\epsilon)^2}}{(1-\epsilon)^2} \right| \quad (20)$$

It is readily apparent that an increase in density in the stagnation region will decrease the shock standoff distance for both theoretical formulas. This behavior will be shown in the tabulated results in Section V. For the Mach numbers considered, the density ratio was calculated from the normal shock relations as tabulated in NACA Report 1135<sup>21</sup>. Anderson has an excellent discussion and derivation of the limiting form of the hypersonic shock relations in Reference 10.

2.5.2. Modified Newtonian Theory. Also in Reference 10, Anderson provides the following historical perspective:

In Propositions 34 and 35 of his Principia, first published in 1687, Newton modeled a fluid flow as a stream of particles in rectilinear motion, much like a stream of pellets from a shotgun blast which, when striking a surface, would lose all their momentum normal to the surface but would move tangentially to the surface without loss of tangential momentum.

This led to the famous newtonian sine-squared law for pressure coefficient

$$C_p = 2\sin^2\theta \quad (21)$$

where  $\theta$  is the local deflection angle of the surface. Anderson also reports the Lester Lees modification to Newtonian theory which gives the pressure coefficient as

$$C_p = C_{p_{MAX}} \sin^2\theta \quad (22)$$

$C_{p_{MAX}}$  is the maximum value of the pressure coefficient, evaluated at a stagnation point behind a normal shock wave given as

$$C_{p_{MAX}} = \frac{p_{t_{stag}} - p_{\infty}}{\frac{1}{2} \rho_{\infty} V_{\infty}^2} \quad (23)$$

where  $p_{t_{stag}}$  is the total pressure behind the normal shock wave at the freestream Mach number. For the Mach numbers considered,  $p_{t_{stag}}$  was determined from the tabulated normal shock relations in NACA Report 1135<sup>21</sup>.

2.5.3. Entropy Jump Condition. The theory presented in this section is from Reference 7. From the second-law of thermodynamics, the entropy always increases across a shock wave. With the assumption of a calorically perfect gas, in which the coefficients of specific heat are constant, the first-law of thermodynamics provides the increase in entropy as

$$\Delta s = c_p \ln\left(\frac{T_{t_{stag}}}{T_{t_\infty}}\right) - R \ln\left(\frac{P_{t_{stag}}}{P_{t_\infty}}\right) \quad (24)$$

where  $\Delta s$  = the change in entropy from freestream to that behind the shock,  $T_t$  = total temperature,  $R$  = gas constant,  $P_t$  = total pressure and the subscripts *Stag* and  $\infty$  represent stagnation and freestream quantities, respectively.

For a stationary normal shock and a non-chemically reacting gas

$$T_{t_{stag}} = T_\infty \quad (25)$$

and Eq (24) becomes

$$\frac{\Delta s}{R} = \ln\left(\frac{P_{t_\infty}}{P_{t_{stag}}}\right) \quad (26)$$

As mentioned in the previous section, NACA Report 1135<sup>21</sup> values were used to determine the pressures and hence the theoretical entropy jump condition.

2.5.4. Shock Impingement on a Sphere. Exact theoretical solutions of the dynamics of a planar moving shock wave striking and passing over a sphere do not exist. Approximate theories due to Whitham and to von Neumann are presented by Bryson and Gross<sup>22</sup> and Heilig<sup>23</sup>, respectively. Their approximate natures only reveal the gross structure of the shock diffraction process. Thus, only qualitative features from these theories can be described. The following qualitative description of the time evolution of the shock-diffraction process for a cylinder or a sphere is taken from Young and Yee<sup>18</sup>, Bryson and Gross<sup>22</sup>, Heilig<sup>23</sup>, Yee and Kutler<sup>24</sup>, and Takayama<sup>25</sup>.

The shock structure at two instances of time,  $t_1$  and  $t_2$ , after initially striking the sphere, is shown in Figure 3. This illustration is for an incident shock of low Mach number with single Mach reflection. When the planar moving shock hits the sphere, regular reflection occurs at the shock impingement point. The reflected shock emerges as a highly curved bow-shock. The shock curvature induces an entropy gradient downstream which, in turn, introduces vorticity into the initially irrotational flowfield. As the shock impingement point propagates around the body, the reflection process transitions from regular reflection to Mach reflection. Depending on the initial strength of the shock wave, complex and double Mach reflection shock structures are

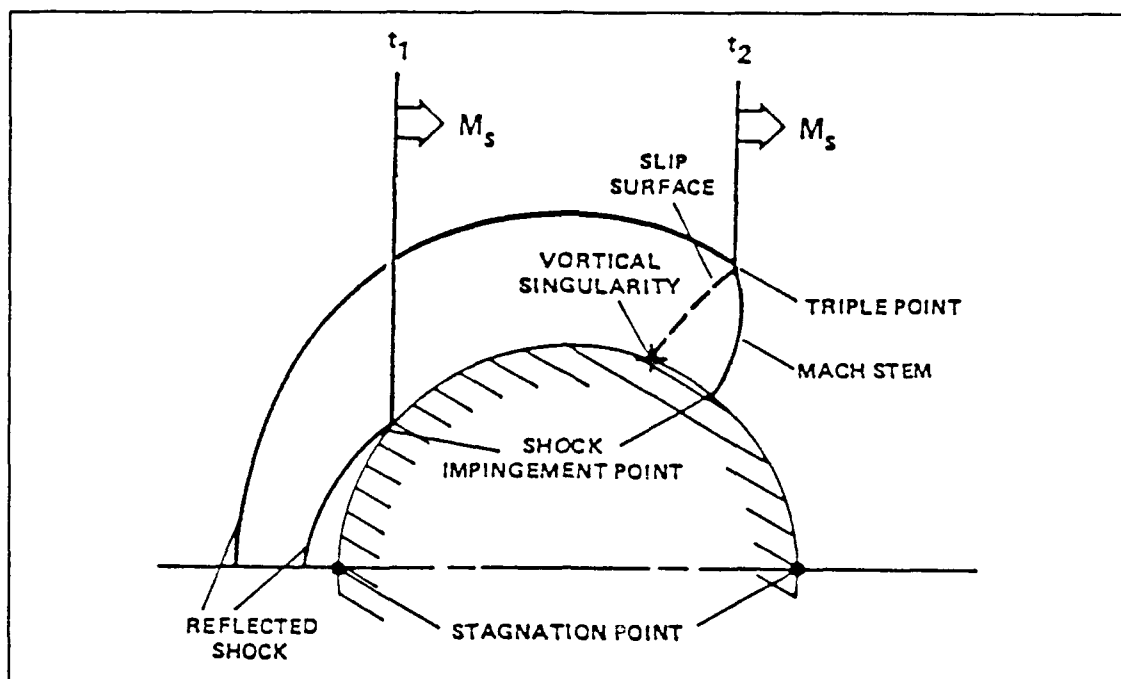


Figure 3. Shock Diffraction Process at Two Instances in Time

also possible during the transition process. For single Mach reflection, a triple point forms and the incident shock no longer touches the body. Three waves emanate from the triple point:

- 1) a Mach stem (strong shock) which impinges normal to the body surface,
- 2) a slip surface or shear layer which strikes the body and results in a vortical singularity (nodal point of streamlines), and
- 3) the reflected shock which moves away from the sphere.

Additionally, a stagnation point (saddle point of streamlines) exists at the lines of axisymmetry, both fore and aft of the sphere.

For double Mach reflection, an irregular reflection occurs in the vicinity of the triple point which causes a

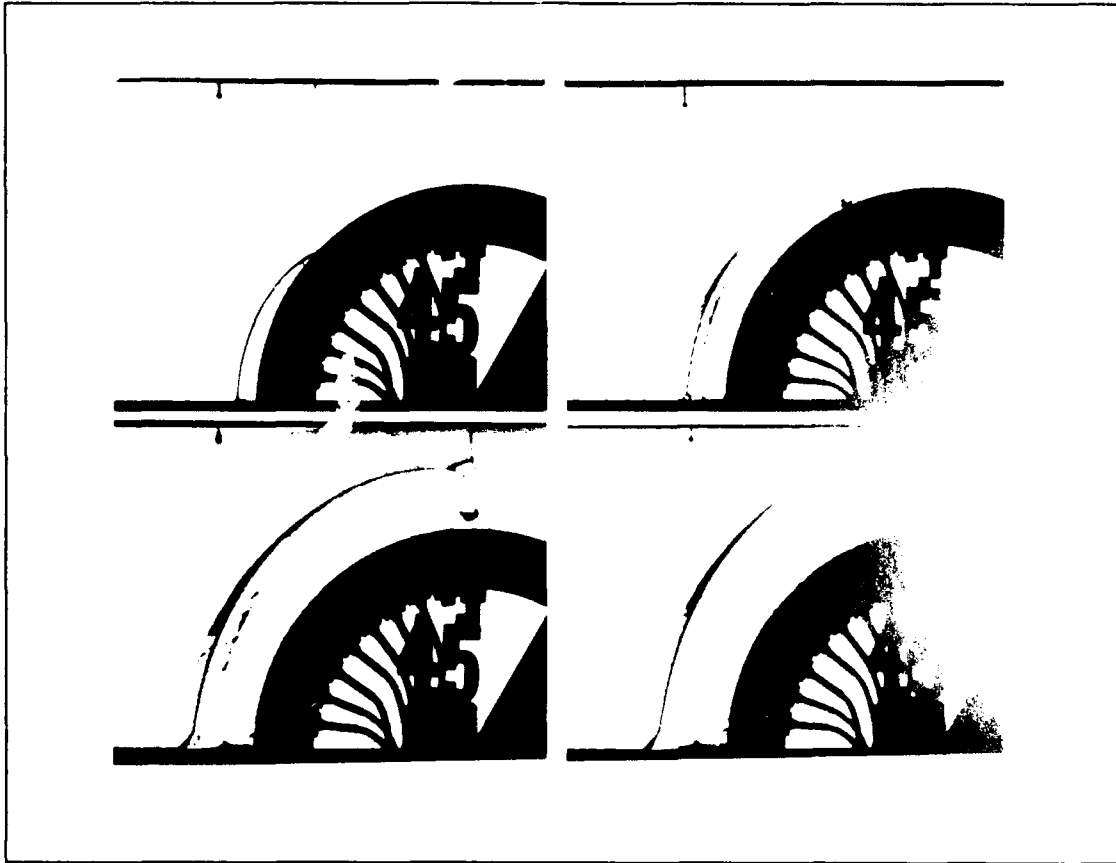


Figure 4. Double Mach Reflection, Mach = 3.36

splitting into two triple points - usually for incident shocks greater than about Mach 1.4. Figure 4 presents a Schlieren photograph from Reference 23 that illustrates this phenomena. Whereas the Mach stem shock is newly created and was not present before, the reflected shock of the irregular reflection phase will interact with the remaining reflected shock of the regular reflection phase. It cannot be assumed that both shocks will go together either in their inclinations or in their strengths. Hence, their intersection appears as a small kink which starts at a new triple point and ends at

the original triple point. If two shocks with unequal slopes interact in two dimensions, a new shock, "the second Mach shock," and a new slip line, "the second slip line", are created. The high-resolution capability of the TVD scheme captures this phenomena as will be shown in Section VI.

## 2.6 Convergence Criteria

One of the convergence criteria for the TVD and the MacCormack scheme was the Euclidean  $L_2$  norm given as

$$L_2 = \left( \sum_{j=1}^J \sum_{i=1}^I (U_{i,j}^{n+1} - U_{i,j}^n)^2 \right)^{\frac{1}{2}} \quad (27)$$

where  $I$  and  $J$  correspond to the maximum number of grid lines in the circumferential and radial directions, respectively, and where  $U_{i,j}$  is the vector of unknowns given by Eq (2). For the steady-state computations, a reduction of the  $L_2$  norm by three to four orders of magnitude from that at the initial state was considered a converged solution. Additionally, the variation of the stagnation pressure and the shock standoff distance was monitored. These values stabilized quickly, and the  $L_2$  norm was the final convergence criterion. For the unsteady shock impingement computations, the  $L_2$  norm was monitored and stable values were of order one.

### III. Experimental Data

For the steady-state blunt-body problem, the experimental data consists of graphical results for shock standoff distance and tabulated results for wave shape and surface pressure distributions about the nose of AGARD Model E, a hemisphere cylinder configuration. The tests were conducted in the von Karman Gas Dynamics Facility (VKF) at the Arnold Engineering Development Center at Mach numbers 3.0, 4.03, 5.06, 6.03, and 8.1 at zero angle of attack. The experimental shock standoff distance and wave shape coordinates were obtained in the report from scaled Schlieren photographs. Model pressures were measured with a system of 15-, 5-, and 1-psid transducers connected to orifices along the body. Figure 5 shows excellent agreement between the experimental surface pressures and that predicted by modified Newtonian theory, Eq (22). Complete details of the test can be obtained in Reference 26.

For the unsteady shock impingement on a sphere, the experimental data for visual comparison consists of Schlieren photographs of the diffraction patterns at a time when the incident shock had passed beyond the aft end of the sphere. "An English table-tennis ball of 1 in. diameter filled with Wood's metal and suspended in the test section from 8 nylon strings was used for a sphere<sup>22</sup>." The tests were conducted at Harvard University with a shock Mach number of 2.89

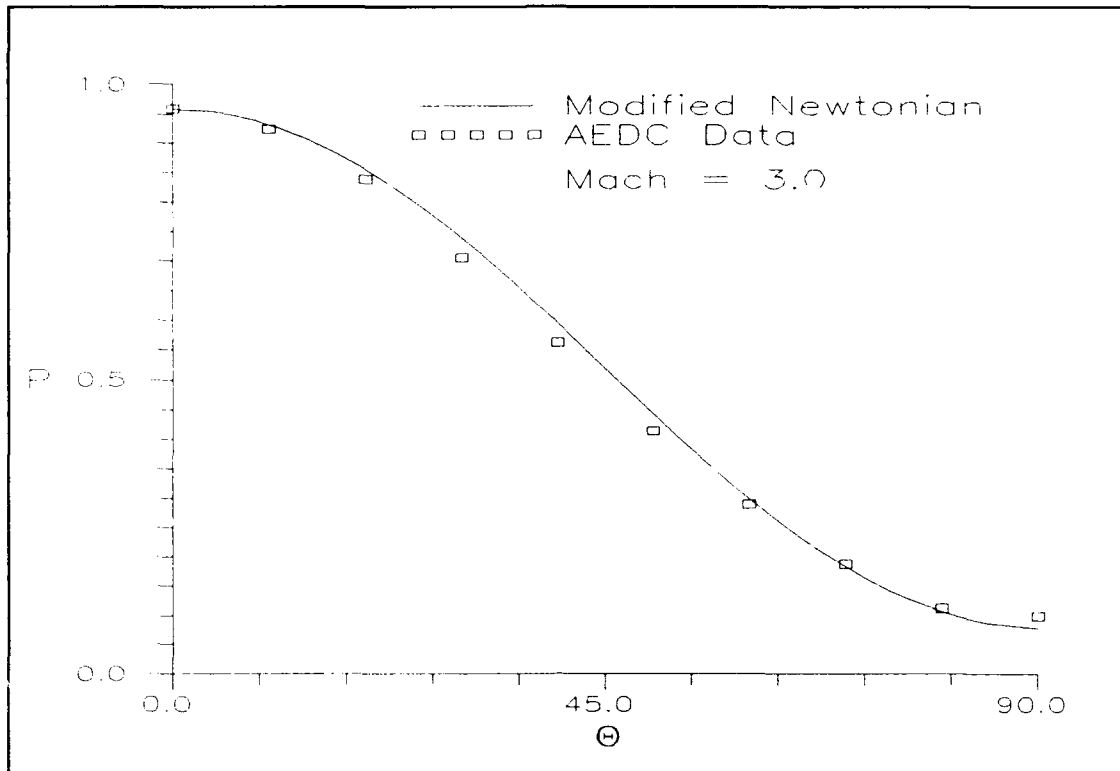


Figure 5. Surface Pressure Distributions, Modified Newtonian Theory and AEDC Data, Mach = 3.0

in a shock tube in air. General features of the shock diffraction process, as discussed in Section 2.5.4, are readily discernible in the Schlieren photographs to be shown in Section VI.

#### IV. Numerical Algorithm Development

An explicit, second-order accurate, upwind, TVD scheme originally developed by Harten and modified by Yee<sup>1</sup> for two-dimensional flow was extended to axisymmetric flow in this study. An excellent review of TVD schemes and their development can be found in Reference 1. Strang time-splitting was used to maintain second-order time accuracy in which the local characteristic solution  $\hat{U}^{n+1}$  is computed from  $\hat{U}^n$  by

$$\hat{U}_{i,j}^{n+1} = L_{\xi}^{h/2} L_{\eta}^h L_{\xi}^{h/2} U_{i,j}^n \quad (28)$$

where  $\xi = i\Delta\xi$ ,  $\eta = j\Delta\eta$ ,  $h = \Delta t$  and

$$\begin{aligned} L_{\xi}^{h/2} \hat{U}_{i,j}^n &= \hat{U}_{i,j}^* = \hat{U}_{i,j}^n - \frac{\Delta t}{\Delta \xi} (\hat{E}_{i+\frac{1}{2},j}^n - \hat{E}_{i-\frac{1}{2},j}^n) \\ L_{\eta}^h \hat{U}_{i,j}^* &= \hat{U}_{i,j}^* - \frac{2\Delta t}{\Delta \eta} (\hat{F}_{i,j+\frac{1}{2}}^* - \hat{F}_{i,j-\frac{1}{2}}^*) + \frac{\Delta t}{\Delta \eta} \hat{S}_{i,j}^* \end{aligned} \quad (29)$$

This sequence of operators is consistent if the sum of the time steps for each of the operators are equal. Second-order time accuracy is obtained if the operators are applied in a symmetric sequence<sup>8</sup>. Furthermore, the time-splitting allows one to handle the homogeneous part of the governing partial differential equations and the source term in separate steps<sup>1</sup>. The functions  $\hat{E}_{i+\frac{1}{2},j}^n$  and  $\hat{F}_{i,j+\frac{1}{2}}^n$  are the numerical

fluxes in the  $\xi$  and  $\eta$  directions, respectively. They are evaluated at cell interfaces and can be written as

$$\begin{aligned}\hat{E}_{i+\frac{1}{2}} &= \frac{1}{2} [\mathcal{E}_i + \mathcal{E}_{i+1} + (R_\xi \Phi)_{i+\frac{1}{2}}] \\ \hat{F}_{j+\frac{1}{2}} &= \frac{1}{2} [\mathcal{F}_j + \mathcal{F}_{j+1} + (R_\eta \Phi)_{j+\frac{1}{2}}]\end{aligned}\quad (30)$$

where (dropping subscripts for notational convenience)

$$\begin{aligned}\mathcal{E} &= y_\eta E - x_\eta F \\ \mathcal{F} &= -y_\xi E + x_\xi F\end{aligned}\quad (31)$$

This formulation has the property of maintaining the freestream, thereby eliminating the problem of delineating physical flowfield structure from aberrations due to the grid<sup>27</sup>. In the discussion of boundary conditions in Section 2.3.1, it was stated that the flux at the line of axisymmetry was set to zero. For the front stagnation line with  $i = 2$  ( $i = 1$  is the ghost point) the  $\xi$  direction numerical flux becomes

$$\hat{E}_{\frac{1}{2}} = \frac{1}{2} (R_\xi \Phi)_{\frac{1}{2}} \quad (32)$$

with no change in the  $\hat{E}_{\frac{3}{2}}$  numerical flux. In the unsteady computations, for the rear stagnation line with  $i = I-1$  ( $i = I$  is the ghost point) the  $\xi$  direction numerical flux becomes

$$\hat{E}_{I-\frac{1}{2}} = \frac{1}{2} (R_\xi \Phi)_{I-\frac{1}{2}} \quad (33)$$

with no change in the  $\hat{E}_{I-\frac{3}{2}}$  numerical flux. Roe's averaging for a perfect gas<sup>11</sup> is used to assess the eigenvalues and

eigenvectors at cell interfaces, because it has the computational advantage of resolving stationary discontinuities<sup>28</sup>. The Roe averaged dependent variables are given by

$$\begin{aligned} u_{i+\frac{1}{2}} &= \frac{Du_{i+1} + u_i}{D + 1} \\ v_{i+\frac{1}{2}} &= \frac{Dv_{i+1} + v_i}{D + 1} \\ H_{i+\frac{1}{2}} &= \frac{DH_{i+1} + H_i}{D + 1} \end{aligned}$$

$$c_{i+\frac{1}{2}}^2 = (\gamma - 1) \left[ H_{i+\frac{1}{2}} - \frac{1}{2} (u_{i+\frac{1}{2}}^2 + v_{i+\frac{1}{2}}^2) \right] \quad (34)$$

where

$$D = \sqrt{\rho_{i+1}/\rho_i} \quad (35)$$

The vector elements of  $\Phi_{i+\frac{1}{2}}$  for the TVD scheme are

$$\phi_{i+\frac{1}{2}}^l = \sigma(v_{i+\frac{1}{2}}^l) (g_{i+1}^l + g_i^l) - \psi(v_{i+\frac{1}{2}}^l + \gamma_{i+\frac{1}{2}}^l) \alpha_{i+\frac{1}{2}} \quad (36)$$

and  $l = 1$  to  $4$  is consistent with Eq (2) and where, with  $\lambda = \Delta t / \Delta x$

$$v_{i+\frac{1}{2}}^l = \lambda a_{i+\frac{1}{2}}^l \quad (37)$$

$\alpha_{i+\frac{1}{2}}$  is the difference of the characteristic variables in the  $\xi$  direction,

$$\alpha_{i+\frac{1}{2}} = R_{i+\frac{1}{2}}^{-1} (U_{i+1} - U_i) \quad (38)$$

The components of  $\alpha$  are given by

$$\begin{bmatrix} \alpha_{i+\frac{1}{2}}^1 \\ \alpha_{i+\frac{1}{2}}^2 \\ \alpha_{i+\frac{1}{2}}^3 \\ \alpha_{i+\frac{1}{2}}^4 \end{bmatrix} = \begin{bmatrix} (aa - bb)/2 \\ \Delta_{i+\frac{1}{2}} \rho - aa \\ (aa + bb)/2 \\ cc \end{bmatrix} \quad (39)$$

where

$$\begin{aligned} aa &= \frac{\gamma-1}{c_{i+\frac{1}{2}}^2} \left[ \Delta_{i+\frac{1}{2}} e + \frac{u_{i+\frac{1}{2}}^2 + v_{i+\frac{1}{2}}^2}{2} \Delta_{i+\frac{1}{2}} \rho - u_{i+\frac{1}{2}} \Delta_{i+\frac{1}{2}} m_x - v_{i+\frac{1}{2}} \Delta_{i+\frac{1}{2}} m_y \right] \\ bb &= \frac{1}{c_{i+\frac{1}{2}}} [k_{h1} \Delta_{i+\frac{1}{2}} m_x - (k_{h1} u_{i+\frac{1}{2}} + k_{h2} v_{i+\frac{1}{2}}) \Delta_{i+\frac{1}{2}} \rho + k_{h2} \Delta_{i+\frac{1}{2}} m_y] \\ cc &= k_{h1} \Delta_{i+\frac{1}{2}} m_y + (k_{h2} u_{i+\frac{1}{2}} - k_{h1} v_{i+\frac{1}{2}}) \Delta_{i+\frac{1}{2}} \rho - k_{h2} \Delta_{i+\frac{1}{2}} m_x \end{aligned}$$

and

$$\Delta_{i+\frac{1}{2}} z = z_{i+1} - z_i \quad (40)$$

The difference of the characteristic variables in the  $\eta$  direction is constructed similarly.

The function  $\gamma_{i+\frac{1}{2}}^l$  is

$$\gamma_{i+\frac{1}{2}}^l = \sigma(\lambda a_{i+\frac{1}{2}}^l) \begin{cases} \frac{(g_{i+1}^l - g_i^l)}{\alpha_{i+\frac{1}{2}}^l} & \alpha_{i+\frac{1}{2}}^l \neq 0 \\ 0 & \alpha_{i+\frac{1}{2}}^l = 0 \end{cases} \quad (41)$$

where

$$\sigma(z) = \frac{1}{2} [\psi(z) - z^2] \quad (42)$$

and

$$\psi(z) = \begin{cases} |z| & |z| \geq \delta_f \\ \frac{(z^2 + \delta_f^2)}{2\delta_f} & |z| < \delta_f \end{cases} \quad (43)$$

The functions  $\sigma$  and  $\psi$  are referred to as the effective numerical viscosity coefficient and the numerical viscosity coefficient, respectively<sup>4</sup>. The functional form of  $\psi$  was developed by Harten in Reference 4. It serves as an entropy correction to  $|z|$  near 0 to prevent an entropy violation which occurs when Eq (42) vanishes. One can view the size of the entropy correction function,  $\delta_f$ , as a measure of the amount of numerical dissipation added.  $\delta_f = 0$  is the least dissipative, and the larger the  $\delta_f$  the more dissipative the scheme becomes. The numerical simulation of hypersonic blunt-body flows is especially sensitive to the magnitude of

the entropy correction function. As reported in Reference 1, Yee suggests the following form employed in this study:

$$(\delta_f)_{i+\frac{1}{2}} = \delta_p (|(u_c)_{i+\frac{1}{2}}| + |(v_c)_{i+\frac{1}{2}}| + c_{i+\frac{1}{2}}) \quad (44)$$

where  $\delta_p$  is the entropy correction parameter and  $u_c$  and  $v_c$  are the contravariant velocities. Additionally, half of the sound speed is from the  $\xi$  direction and the other half is from the  $\eta$  direction. The function  $\delta_f$  depends on the spectral radius of the Jacobian matrices of the fluxes and is very useful in terms of stability and convergence rate. Yee recommends  $0.05 \leq \delta_p \leq 0.25$  for  $4 \leq M_\infty \leq 25$ . For the nondimensional quantities employed in this study, a consistent value for  $\delta_p$  of 5.0 was used unless indicated otherwise. It should be pointed out that smaller values slow down convergence for the steady-state problem. As mentioned previously, larger values of  $\delta_f$  add more numerical dissipation. An investigation of these effects was conducted and  $3.5 \leq \delta_p \leq 5.5$  was found to work quite well. Values lower than 5.0 dramatically slowed down the convergence rate with only a slight increase in the resolution of the shock as will be shown in Section V. For instance, after 1000 iterations, a value of 5.0 reduced the  $L_2$  norm three orders of magnitude. A value of 4.0 for the same number of iterations did not reduce the  $L_2$  norm a single order of magnitude.

The function  $g_j^l$  is the 'limiter' function which also controls the amount of numerical dissipation added. Hypersonic blunt-body flows with strong shock waves require the proper selection of limiters. The limiter function has been expressed in a number of different ways<sup>1</sup>. This study incorporates limiters appropriate for the characteristic fields under investigation as recommended by Yee<sup>1</sup>. The nonlinear fields correspond to  $l = 1$  and  $l = 3$  and these waves are either shocks or rarefaction waves. For the nonlinear fields,  $a^l R^l \neq 0$ , use

$$g_i^l = (\alpha_{i+\frac{1}{2}}^l \alpha_{i-\frac{1}{2}}^l + |\alpha_{i+\frac{1}{2}}^l \alpha_{i-\frac{1}{2}}^l|) / (\alpha_{i+\frac{1}{2}}^l + \alpha_{i-\frac{1}{2}}^l) \quad (45)$$

The linearly degenerate fields correspond to  $l = 2$  and  $l = 4$  and are uniquely contact discontinuities<sup>4</sup>. For the linearly degenerate fields,  $a^l R^l = 0$ , use

$$g_i^l = \minmod(\alpha_{i-\frac{1}{2}}^l, \alpha_{i+\frac{1}{2}}^l) \quad (46)$$

where the *minmod* function of a list of arguments is equal to the smallest number in absolute value if the list of arguments is of the same sign, or is equal to zero if any arguments are of opposite sign. Limiters other than Eq (46) can produce sharper discontinuities, but are not as robust. For the

unsteady shock impingement problem, the following limiter was used for the linearly degenerate fields

$$g_i^l = S \cdot \max[0, \min(2|\alpha_{i+\frac{1}{2}}^l|, S \cdot \alpha_{i-\frac{1}{2}}^l), \min(|\alpha_{i+\frac{1}{2}}^l|, 2S \cdot \alpha_{i-\frac{1}{2}}^l)] \quad (47)$$

where

$$S = \text{sgn}(\alpha_{i+\frac{1}{2}}^l) \quad (48)$$

A numerical investigation of the differences in resolution of flowfield discontinuities with these limiters will be presented in Section VI. Finally, note that zeroth-order extrapolation is used to obtain limiter values at ghost points.

## V. Steady-State Solutions of the Euler Equations

Steady-state solutions obtained with the TVD and the MacCormack schemes are presented in this section.

### 5.1 Computational Grid

Steady-state solutions were computed using the grid shown in Figure 6. The grid consisted of 51 points in the circumferential direction ( $I = 51$ ) and 25 points in the radial direction ( $J = 25$ ). The body radius,  $R_B$ , was scaled to a nondimensional unit of 1. The spacing in the circumferential direction at the line of axisymmetry was  $.02 R_B$ , and the spacing in the radial direction was  $.01 R_B$ . A geometric progression was used to control the radial spacing from the body surface to the outer boundary and for the circumferential spacing from the line of axisymmetry to the rear outflow boundary. This allowed for clustering of node points in the stagnation region. The location of the far-field boundary was set to  $-1.4 R_B$  along the line of axisymmetry and an outer boundary with a parabolic shape was used.

### 5.2 Shock Standoff Distance and Wave Shape

To evaluate the performance of the TVD and MacCormack schemes, comparisons of shock standoff distance and bow-shock shape were made to theory and to experimental data. To determine the shock standoff distance predicted by the

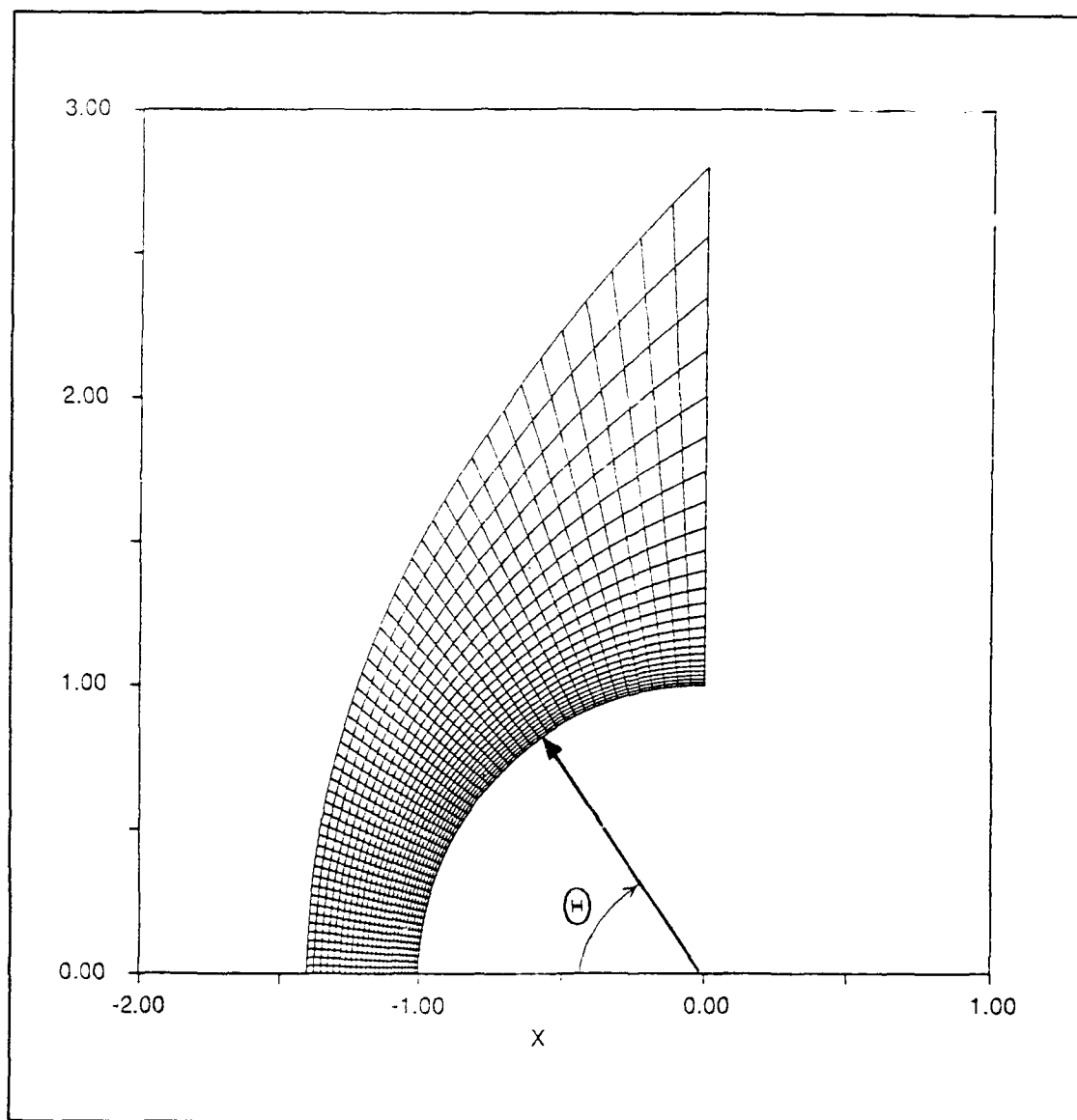


Figure 6. Computational Grid, 51 x 25

schemes, plots of pressure along the line of axisymmetry were used. An example of such a plot for the Mach 3.0 case is shown in Figure 7. Note that the TVD data is from cell centers and the MacCormack data is from node points. These expanded scale plots allow for an interpolation of the data to

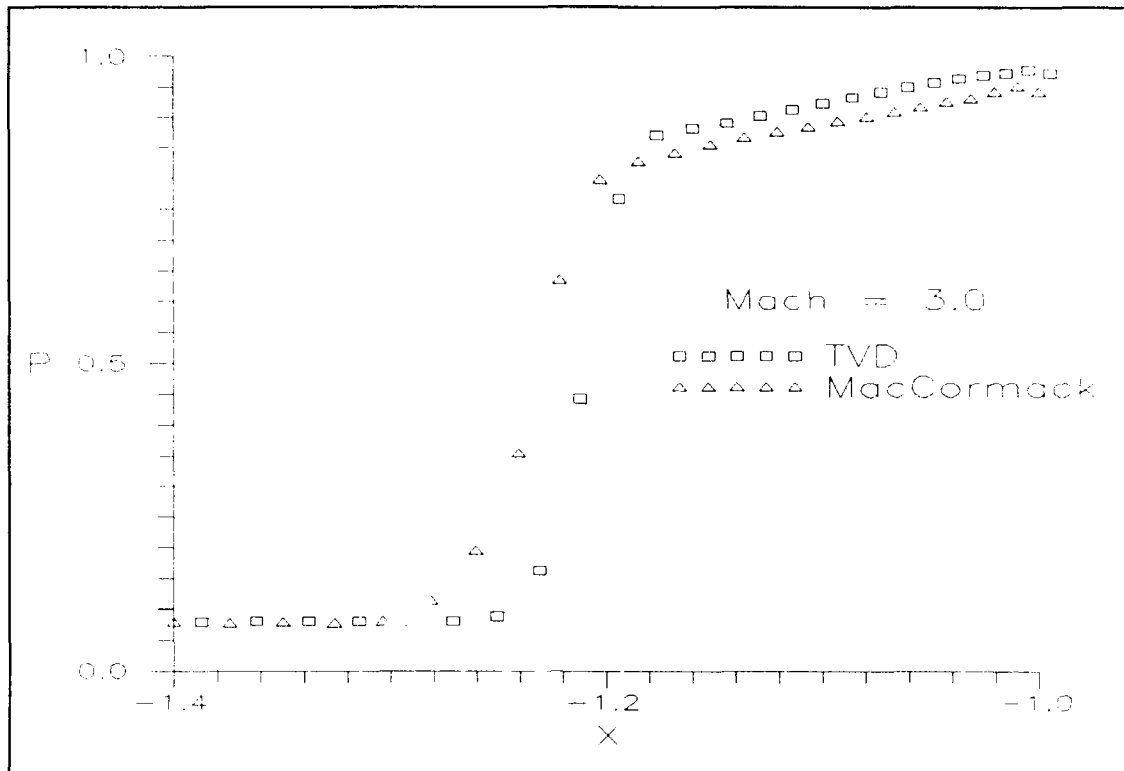


Figure 7. Pressure Along the Line of Axisymmetry, Second-Order TVD and MacCormack Schemes, Mach = 3.0

determine the shock standoff distance. In Figure 7, note that the TVD scheme resolves the shock in fewer grid points than the MacCormack scheme. Typically, TVD schemes do much better than this. It was mentioned in Section IV that the entropy correction parameter,  $\delta_p$ , affected the amount of numerical dissipation added and, in turn, the resolution of shocks. Values for  $\delta_p$  less than 5.0 tended to align the two points around the shock with the pre- and post-shock values. The net result was resolution of the shock in a couple of grid points. However, the penalty paid was a dramatic decrease in the convergence rate. For this study, the efficient calculation

of solutions was a primary concern to the author. Most of the numerical simulations were done interactively in a few thousand iterations at most. Figure 8 shows a contour plot of the entropy correction function given by Eq (44) for the Mach 3.0 case. It appears that the magnitude of the function is related to "position" in the physical domain. That is,  $\delta_f$  is greater near the line of axisymmetry and decreases in the vicinity of the shock where the shock strength decreases. Figure 9 compares pressure plots along the line of axisymmetry from the first-order TVD scheme to the second-order scheme for the Mach 3.0 case. Note that the first-order TVD scheme resolves the shock very well. However, the first-order scheme does not do so well in the region between the shock and the stagnation point.

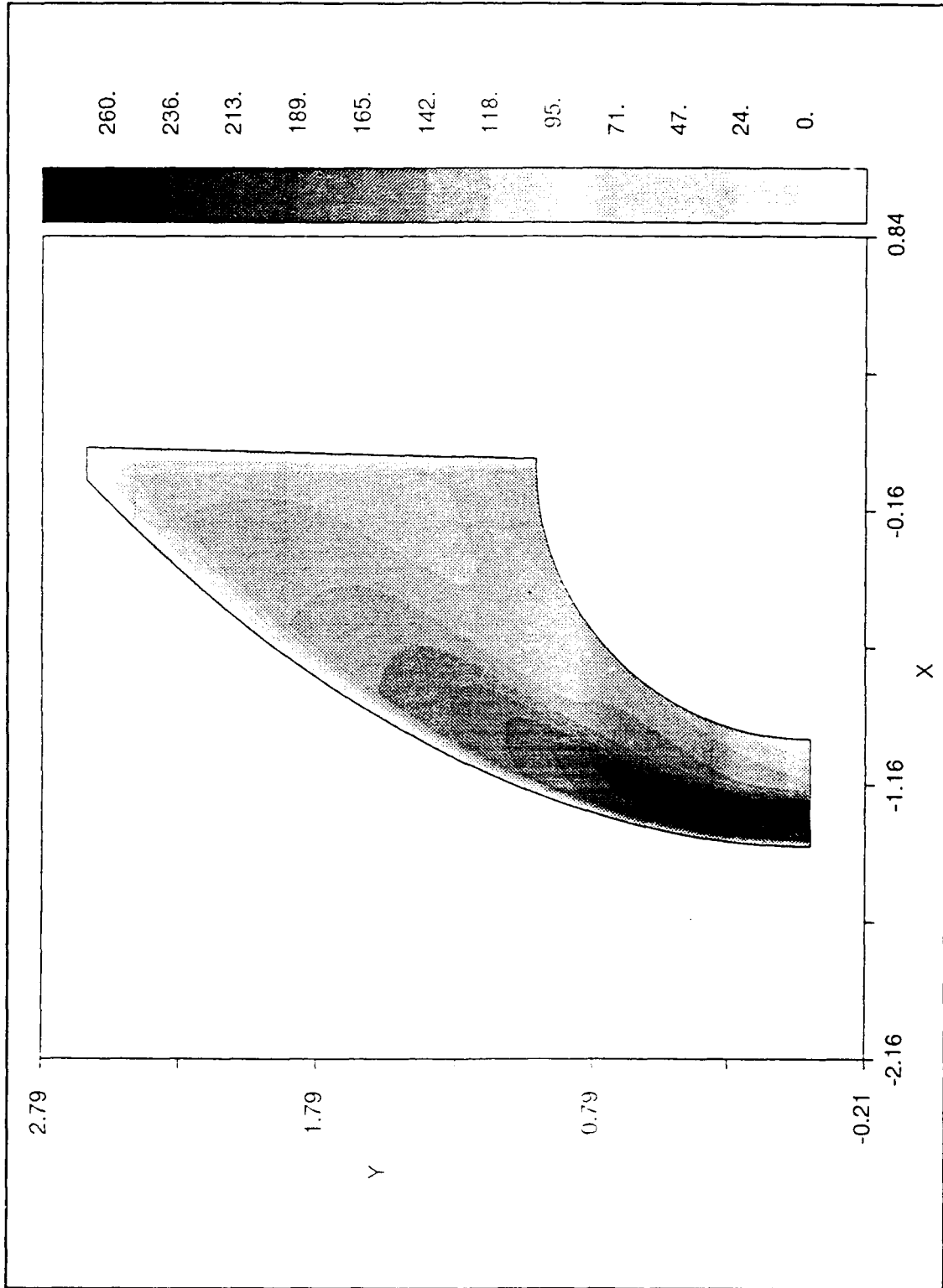


Figure 8. Entropy Correction Function Contours, Mach = 3.0

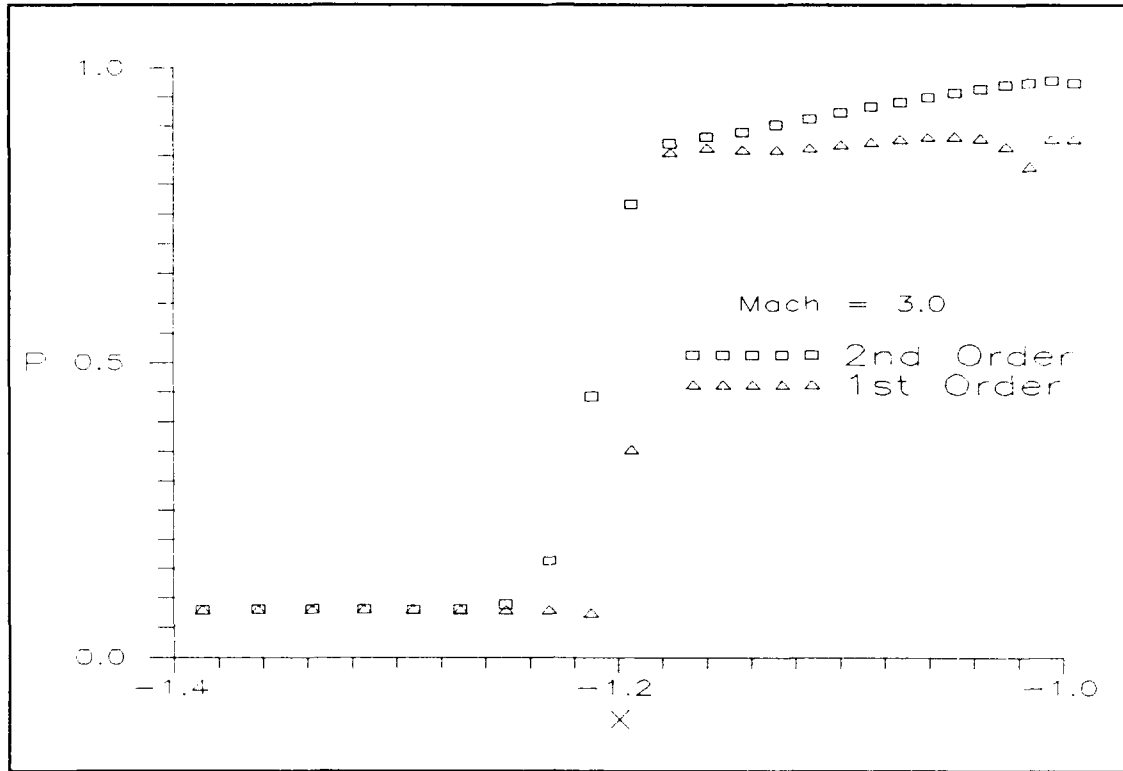


Figure 9. Pressure Along the Line of Axisymmetry, First- and Second-Order TVD Schemes, Mach = 3.0

Table 1 presents a comparison of the calculated shock standoff distances to theory from Section 2.5.1 and AEDC experimental data.

Table 1  
Shock Standoff Distance  
 $\delta_o/R_s$

Mach=>	3.0	4.03	5.06	6.03	8.1
TVD	.177	.144	.132	.126	.121
Eq(19)	.151	.131	.122	.117	.106
Eq(20)	.155	.134	.125	.119	.107
AEDC	.179	.138	.126	.122	--

The TVD and MacCormack schemes compare quite well with theory and experimental data over a wide range of Mach numbers. It should also be pointed out that for the experimental data the shock standoff distances were given in graphical form. Hence, the three significant figures shown are uncertain.

The bow-shock shape was also predicted quite well by both the TVD and MacCormack schemes. Figures 10 and 11 present Mach contours - with the shock coordinates from the tabulated experimental data superimposed - from the TVD and MacCormack schemes, respectively. The TVD scheme Mach contours are much "crisper" than those of the MacCormack scheme, especially in the stagnation region. Also, smoother Mach contours at the outflow boundary are obtained with the TVD scheme as shown in Figure 10. This graphically illustrates the point made in Section 2.3.3 concerning two-point extrapolation as opposed to a "no-change" condition as the outflow boundary condition.

Figure 12 presents Mach contours from the TVD solution at a Mach number of 8.1. Compare this to Figure 10 and the statement from Anderson<sup>10</sup>:

...as  $M_\infty$  increases, the shock wave moves closer to the body and the sonic points on both the shock and the body move closer to the centerline - all standard physical behavior for blunt-body flows. Furthermore, observe that, as  $M_\infty$  increases, the sonic point on the shock moves down faster than the sonic point on the body, and thus the sonic line actually rotates in a counterclockwise fashion as the Mach number increases.

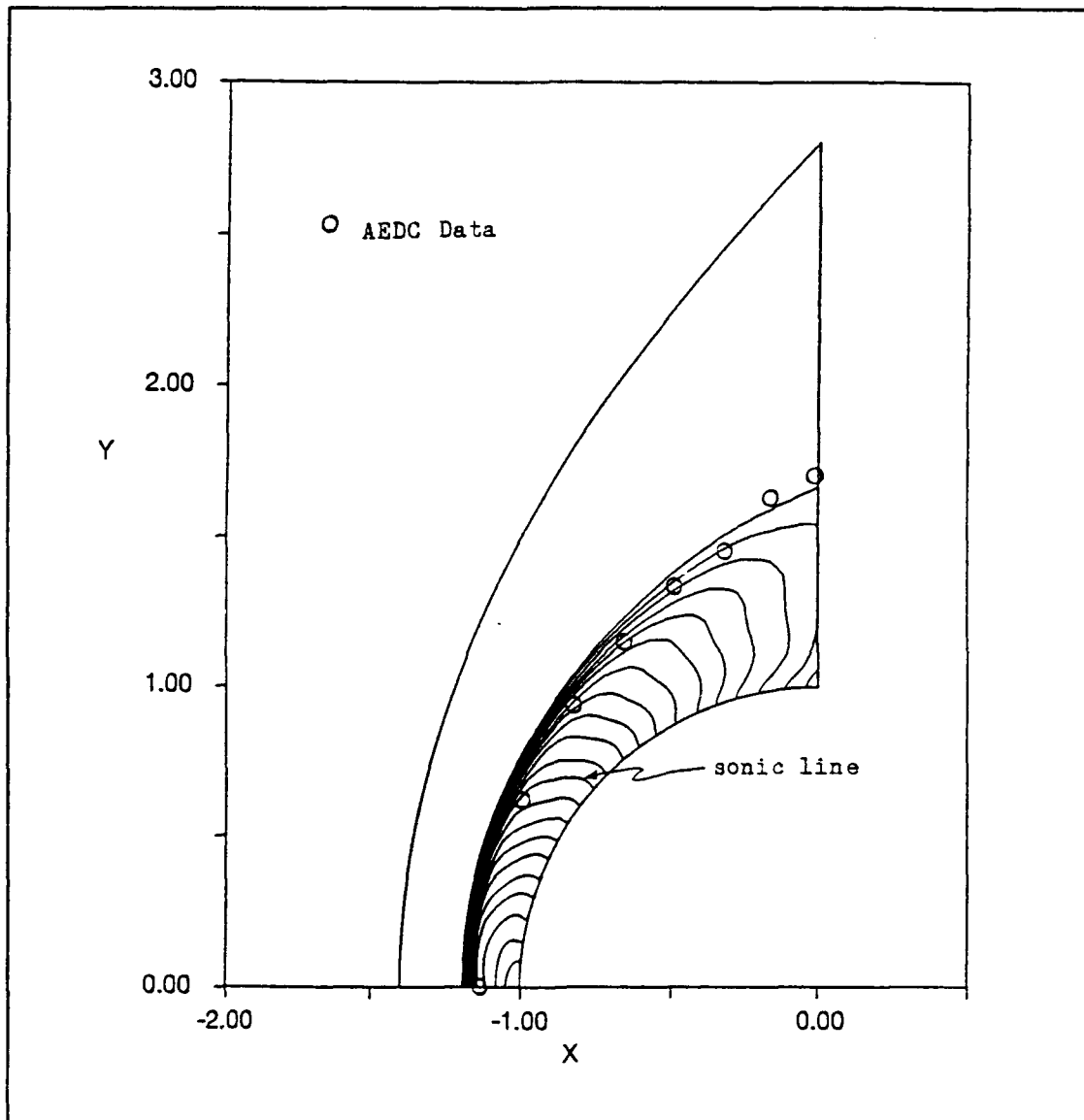


Figure 10. Mach Contours, TVD Scheme, Mach = 4.03

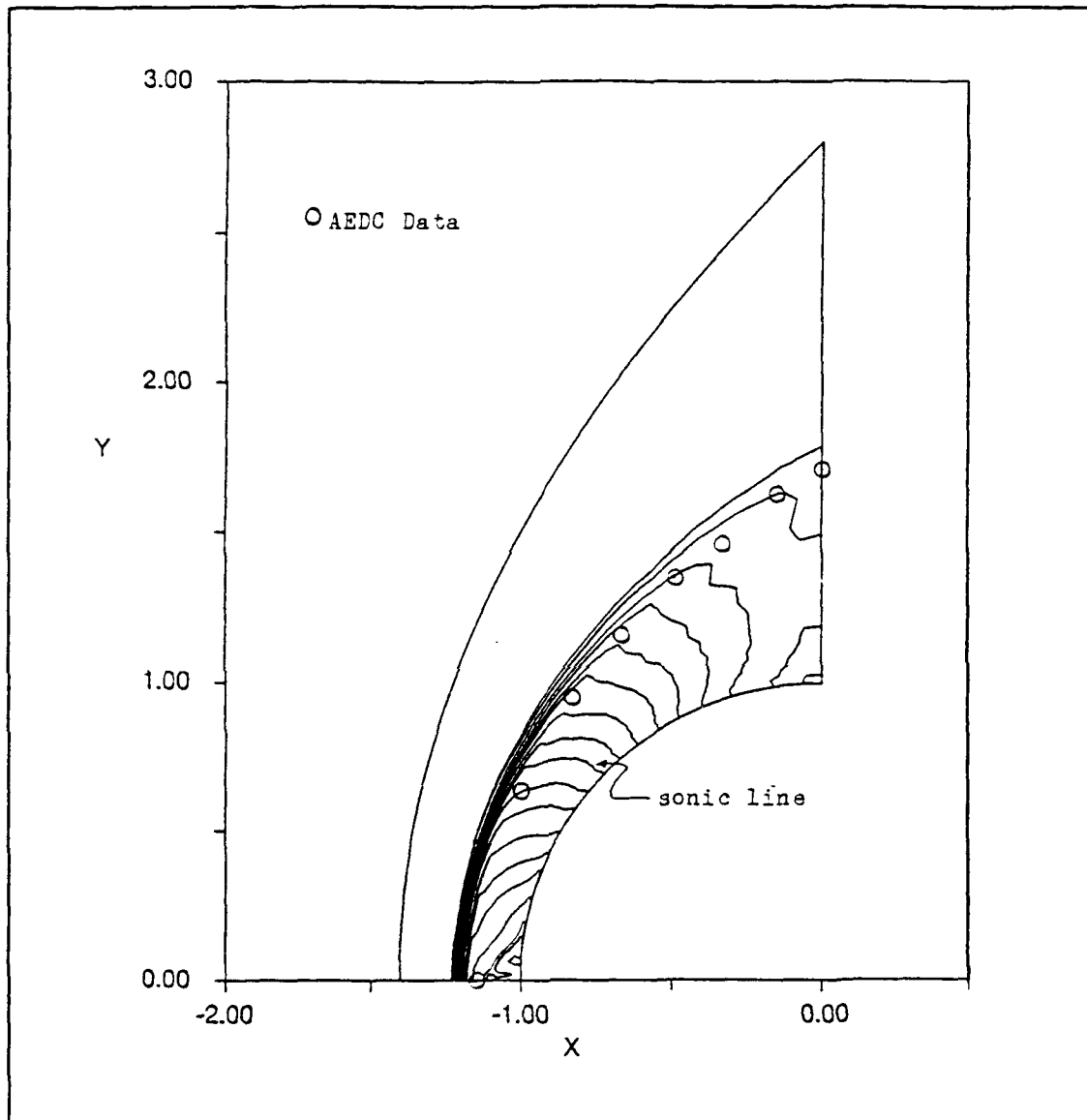


Figure 11. Mach Contours, MacCormack Scheme, Mach = 4.03

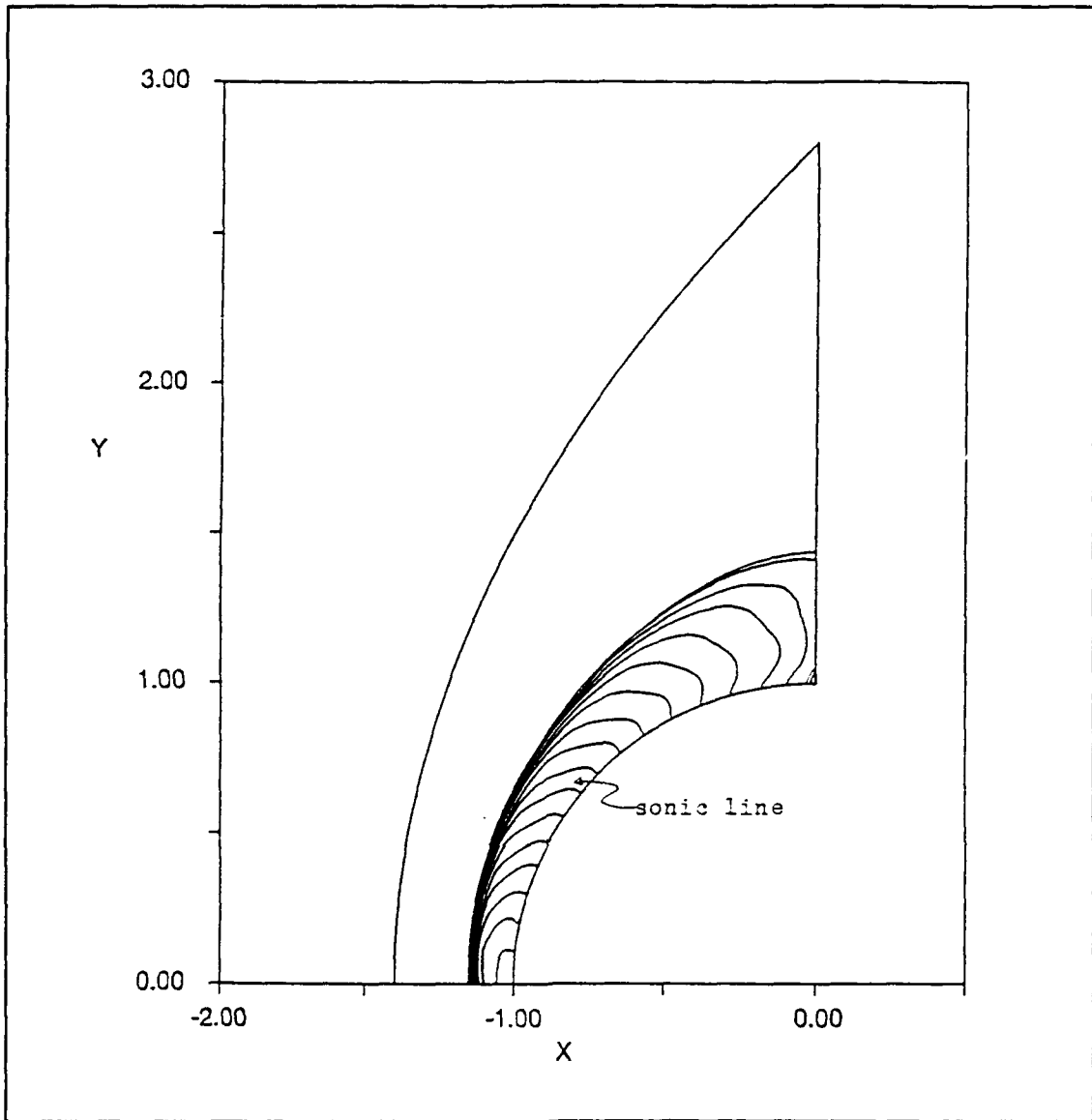


Figure 12. Mach Contours, TVD Scheme, Mach = 8.1

Furthermore, for two-dimensional flow about a cylinder, the angle that the sonic line makes with the body surface remains acute - no matter how high the Mach number. For axisymmetric flow about a sphere, that angle is acute at low Mach numbers and becomes obtuse for Mach numbers approximately greater than

3.0. Figures 10 and 12 demonstrate that the axisymmetric TVD scheme correctly models this physical behavior.

### 5.3 Pressure Distribution

To assess the performance of the TVD and MacCormack schemes, numerically predicted surface pressure distributions are compared to experimental data.

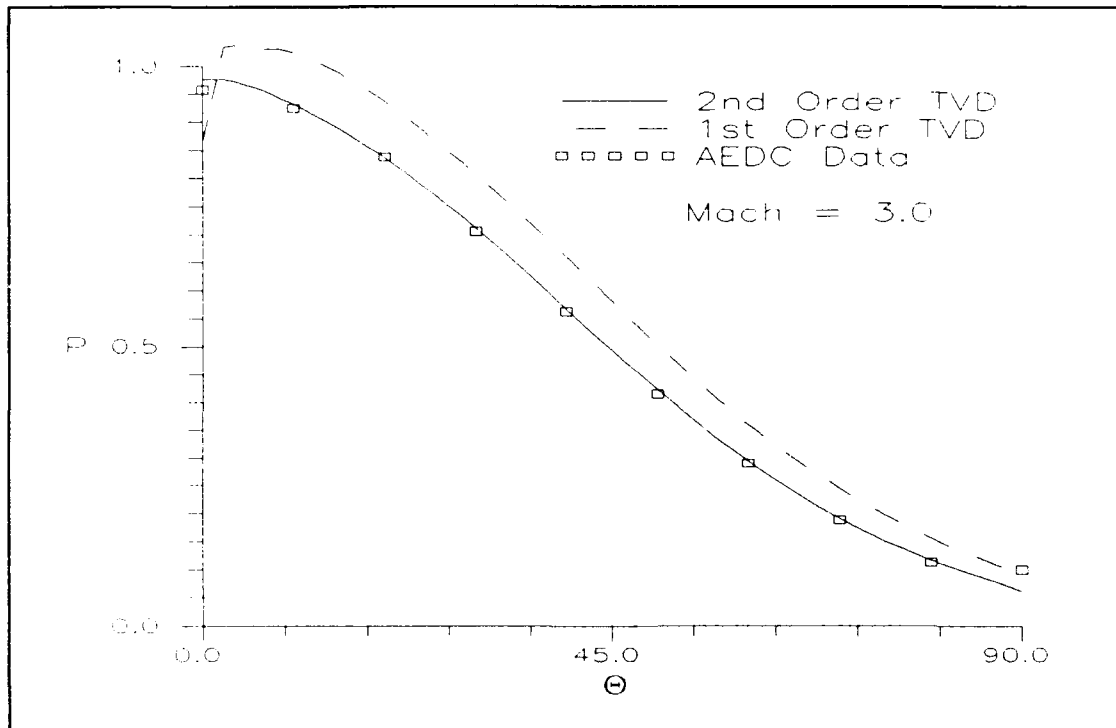


Figure 13. Surface Pressure Distribution, First- and Second-Order TVD Schemes, Mach = 3.0

Figure 13 presents pressure distribution calculations from the first- and second-order TVD schemes compared to the experimental data at Mach 3.0. The solution procedure was; run the first-order TVD scheme for 500 iterations at a CFL number of 0.9, use that solution as an initial state for the

second-order TVD scheme, and run the second-order TVD scheme for as many iterations necessary (usually 500 to 1000) at a CFL number of 0.5 until convergence. Convergence criteria were presented in Section 2.6. In Figure 13, the first-order TVD scheme solution has a pressure oscillation in the stagnation region which underpredicts the stagnation pressure and the scheme overpredicts the pressure distribution. The second-order TVD scheme solution completely damps out the oscillatory behavior and there is excellent agreement with the experimental data. Similar results were obtained for Mach

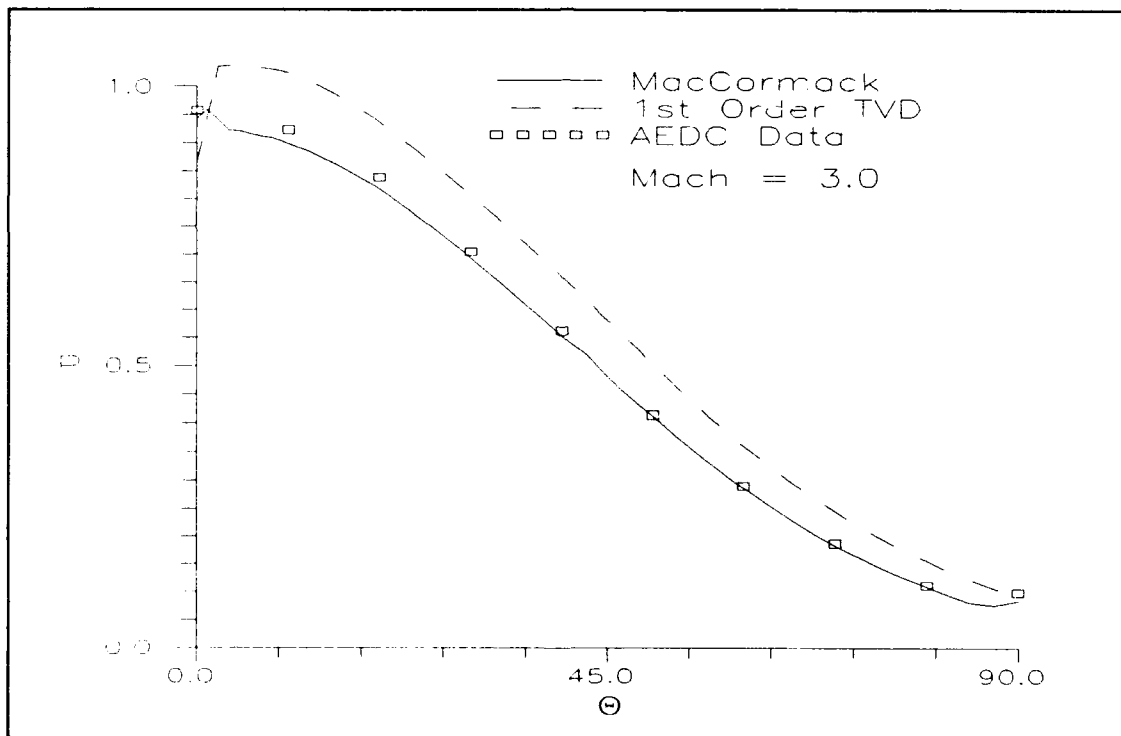


Figure 14. Surface Pressure Distribution, MacCormack and First-Order TVD Schemes, Mach = 3.0

numbers of 4.03, 5.06, 6.03, and 8.1. Figure 14 presents a pressure distribution calculation from the MacCormack scheme

compared to the experimental data at Mach 3.0. This solution was obtained in 10,000 iterations with a CFL number of 0.5. It was not possible to reduce the  $L_2$  norm convergence criterion as low as that obtained with the TVD scheme. At Mach numbers greater than 3.0, it was necessary to reduce the CFL number to no more than 0.1 for stability. Furthermore, after a few thousand iterations, an unphysical recirculation region would develop in the stagnation region, resulting in an accentuated bulge in the bow-shock shape and large pressure oscillations about the stagnation point. This type of behavior in the MacCormack scheme for the blunt-body problem has been reported by Shang and Josyula<sup>6</sup>. In fact, the accentuated bulge looks like an unsteady shock boundary layer interaction ahead of a forward facing step as reported by Saida et al<sup>29</sup>. The causes for this behavior are not completely understood. To eliminate the possibility that the initial state caused this behavior in the MacCormack scheme, a smooth initial state was developed as described in Section 2.4.1. Unfortunately, the recirculation region also developed from this initial condition. An example of the onset of this behavior is shown in Figure 15.

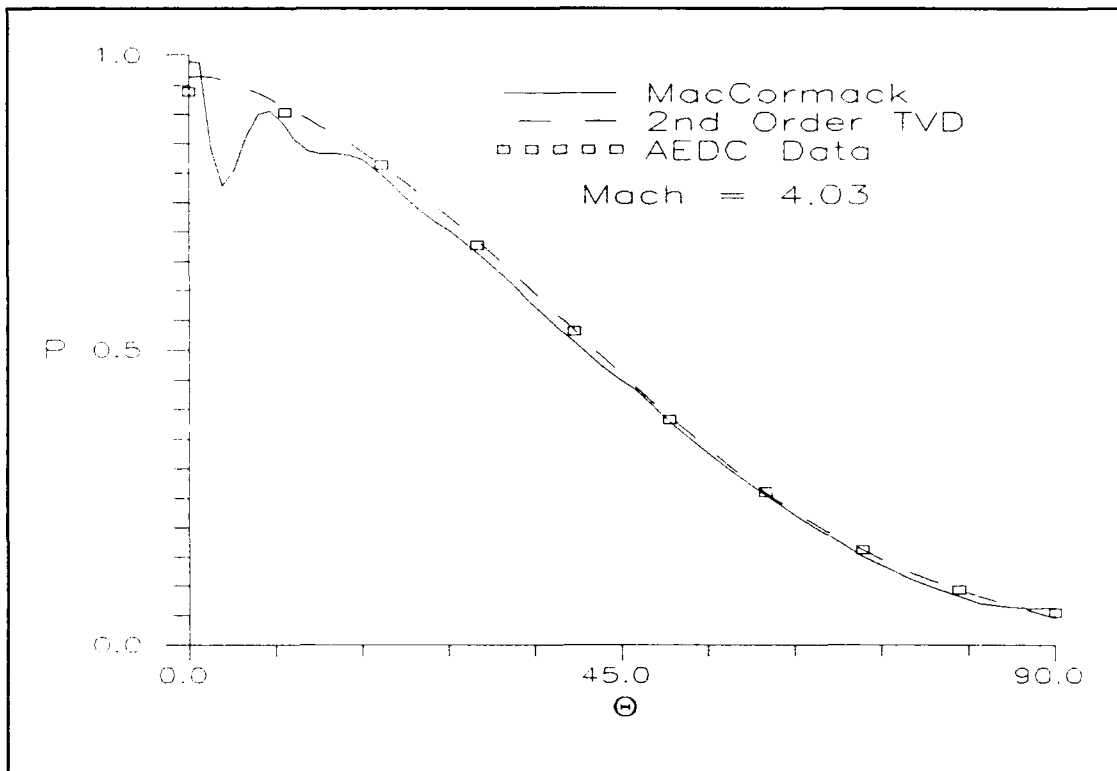


Figure 15. Surface Pressure Distribution, MacCormack and Second-Order TVD Schemes, Mach = 4.03

#### 5.4 Entropy Jump Condition

It is well known that not all algorithms for the Euler equations will compute the physically correct solution and that an entropy condition is required to pick out the relevant solution<sup>30</sup>. The level of spurious entropy produced in the stagnation region of a blunt-nosed configuration is a good measure of a numerical scheme's accuracy<sup>31</sup>.

Table 2 compares theoretical results to that obtained with the second-order TVD and MacCormack scheme.

Table 2  
Entropy Jump Condition  
 $\Delta s/R$

Mach=>	3.0	4.03	5.06	6.03	8.1
Eq(26)	1.114	2.001	2.831	3.539	4.825
TVD	1.095	1.977	2.805	3.511	4.791
%Error	-1.73	-1.18	- .93	- .78	- .70
Mac	1.133	2.027	2.875	3.579	--
%Error	+1.60	+1.30	+1.55	+1.14	--

Excellent agreement is obtained between the TVD scheme and theory. The MacCormack scheme results are also quite good, but stagnation point pressure oscillations were evident, and the  $L_2$  norm had only been reduced two orders of magnitude with the very restrictive CFL number necessary for stability. Further iterations resulted in diverging behavior as mentioned in the previous section.

## VI. Dynamic Solutions of the Euler Equations

The complex unsteady flowfield generated by the impingement of a planar shock on a sphere is a good test case for assessing the time accuracy and shock-capturing capability of the second-order TVD and MacCormack schemes. A discussion of the time evolution of the shock diffraction process was given in Section 2.5.4. Flowfield patterns, specifically density and pressure contours, at different instances in time for the Mach 2.89 case will be presented in the next two sections. A comparison of limiter effects on the resolution of the flowfield structure will also be presented. Additionally, comparison to Schlieren photographs from the Bryson and Gross<sup>22</sup> experiments will be shown.

### 6.1 Computational Grid

The numerical simulations were obtained on the cylindrical grid shown in Figure 16. The grid consisted of 251 evenly spaced points in the circumferential direction and 101 points in the radial direction. The spacing in the radial direction off the body was  $.01 R_b$  and a geometric progression was used to control the spacing from there to the outer boundary. The outer boundary had a radius of 2 body diameters.

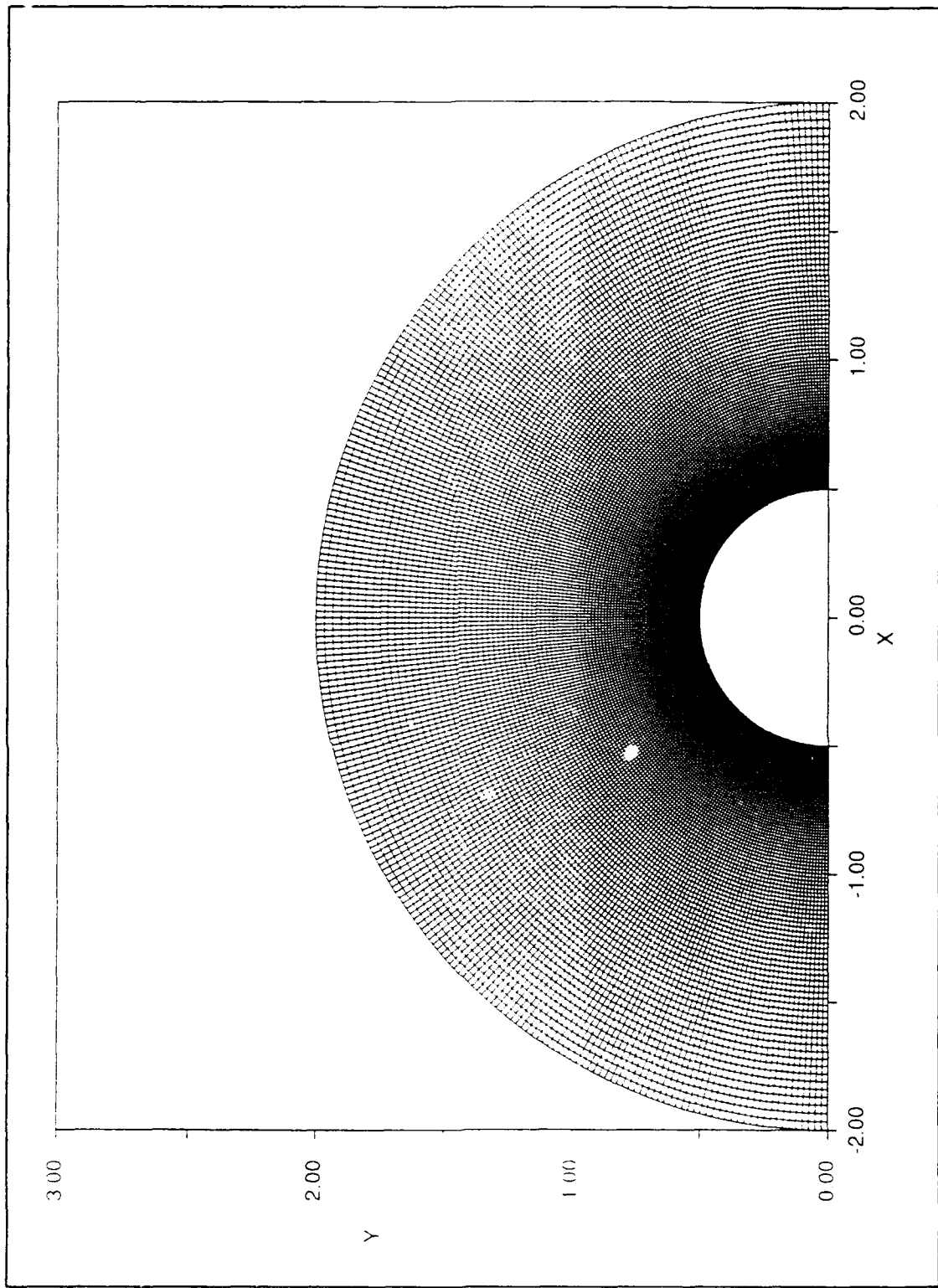


Figure 16. Computational Grid, 251 x 101

## 6.2 Pressure and Density Flowfield Predictions

The numerical simulations were started with the planar shock located at  $x = -0.75$  with a shock Mach number of 2.89. Pre- and post-shock conditions are imposed to the right and left, respectively, of the shock location.

Figures 17 and 18 are density and pressure contours, respectively, at selected times in the shock diffraction process for the TVD scheme. The limiter used for the linear fields was given as Eq (47). The linearly degenerate fields are uniquely contact discontinuities as described in Section IV. Figures 19 and 20 are density and pressure contours, respectively, at approximately the same selected times in the shock diffraction process, for the MacCormack scheme.

Figures 17a, 18a, 19a, and 20a show the reflected shock propagating away from the front of the sphere with the incident shock attached to the body surface at the impingement point. Note the smoother contours for the TVD scheme results.

In Figures 17b, 18b, 19b, and 20b, the impingement point has evolved into the split triple point of a double Mach reflection. This is barely discernible as the kink in the reflected shock - incident shock intersection. Double Mach reflection involves double Mach stems and slip surfaces (contact discontinuities). These will be referred to as primary and secondary for the "upstream" and "downstream" locations.

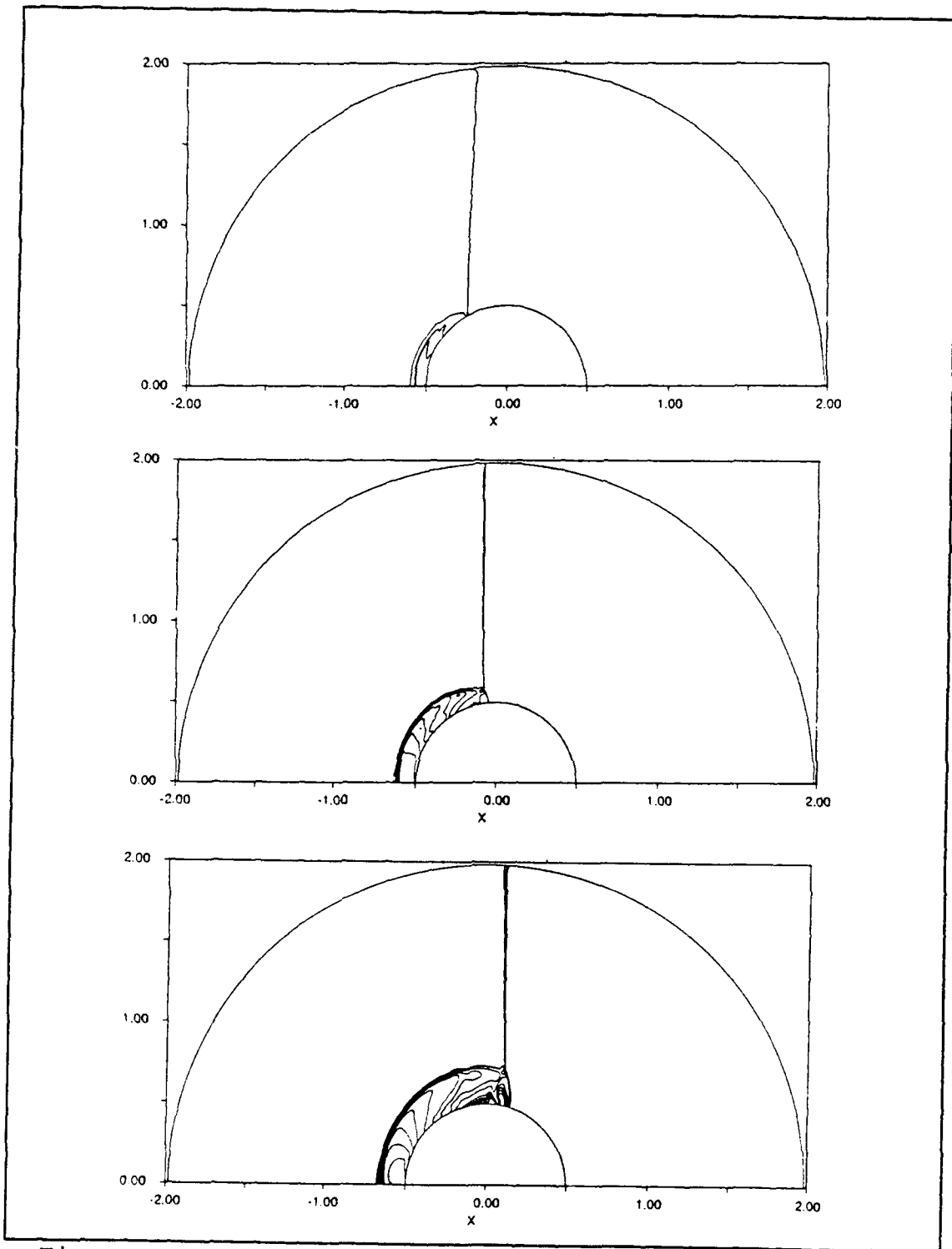


Figure 17. Density Contours, Second-Order TVD Scheme,  
 Time = a) .4924, b) .6727, c) .8703

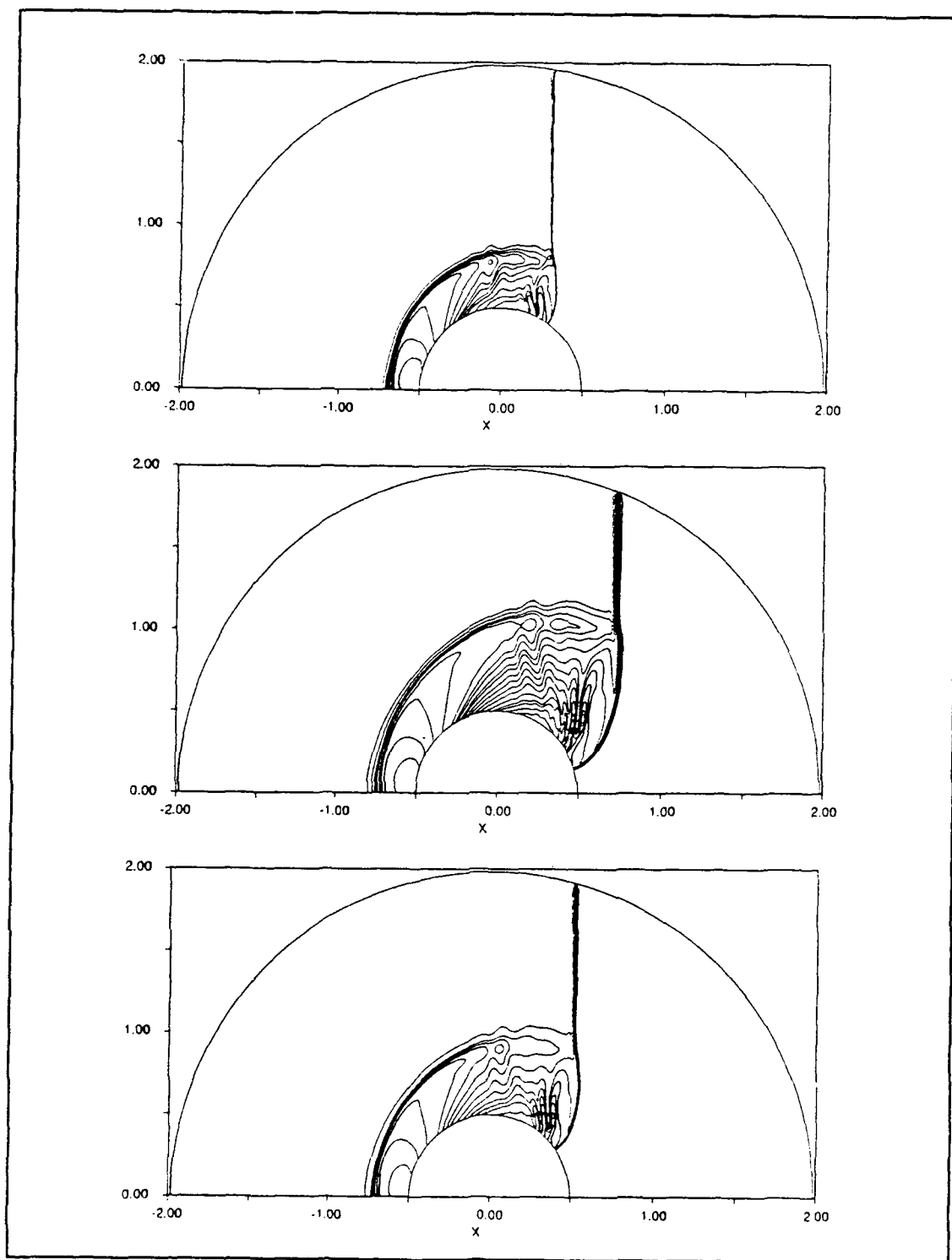


Figure 17. Density Contours, Second-Order TVD Scheme,  
 Time = d) 1.0667, e) 1.2708, and f) 1.4765

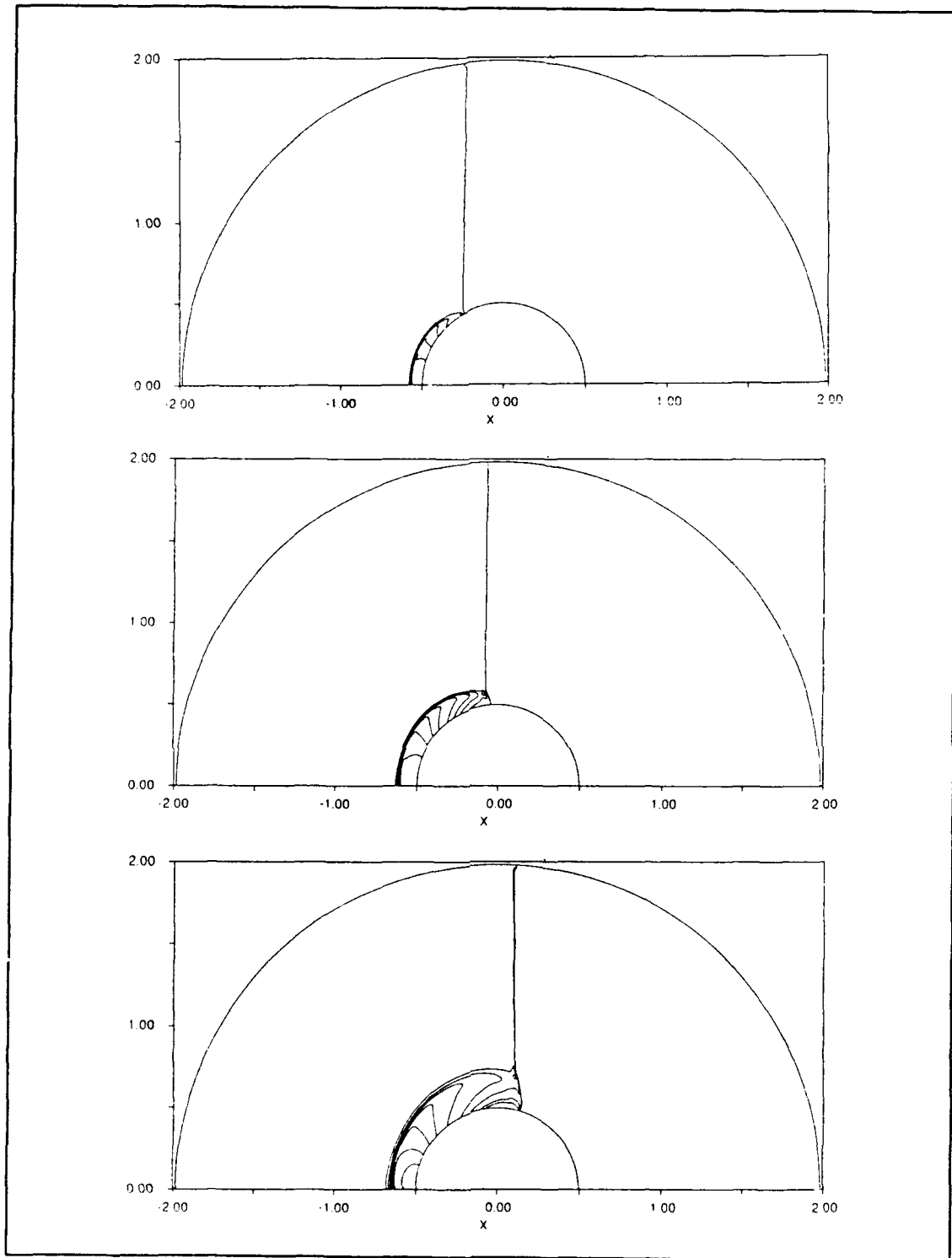


Figure 18. Pressure Contours, Second-Order TVD Scheme,  
Time = a) .4924, b) .6727, c) .8703

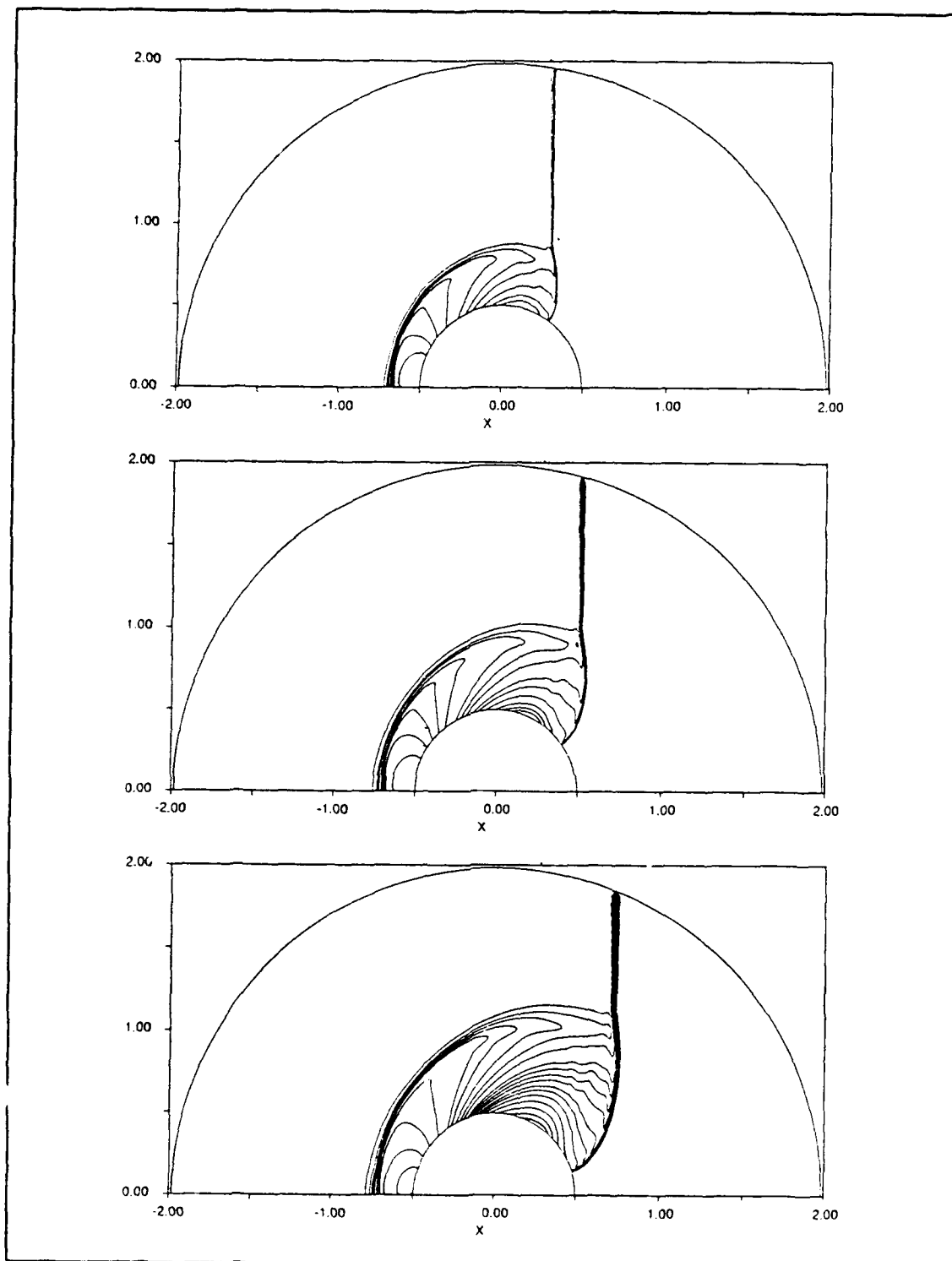


Figure 18. Pressure Contours, Second-Order TVD Scheme,  
 Time = d) 1.0667, e) 1.2708, and f) 1.4765

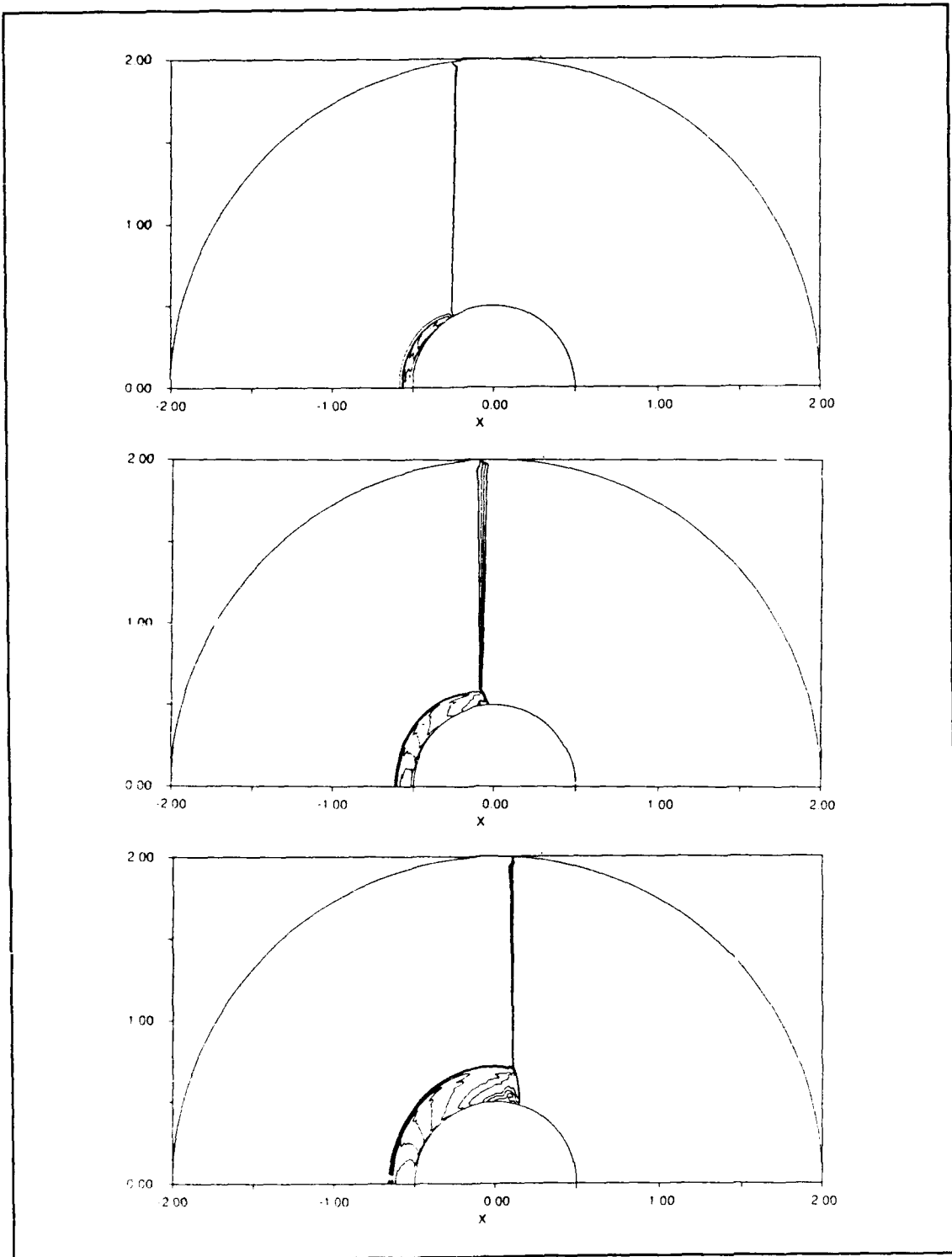


Figure 19. Density Contours, MacCormack Scheme,  
 Time = a) .4901, b) .6706, c) .8679

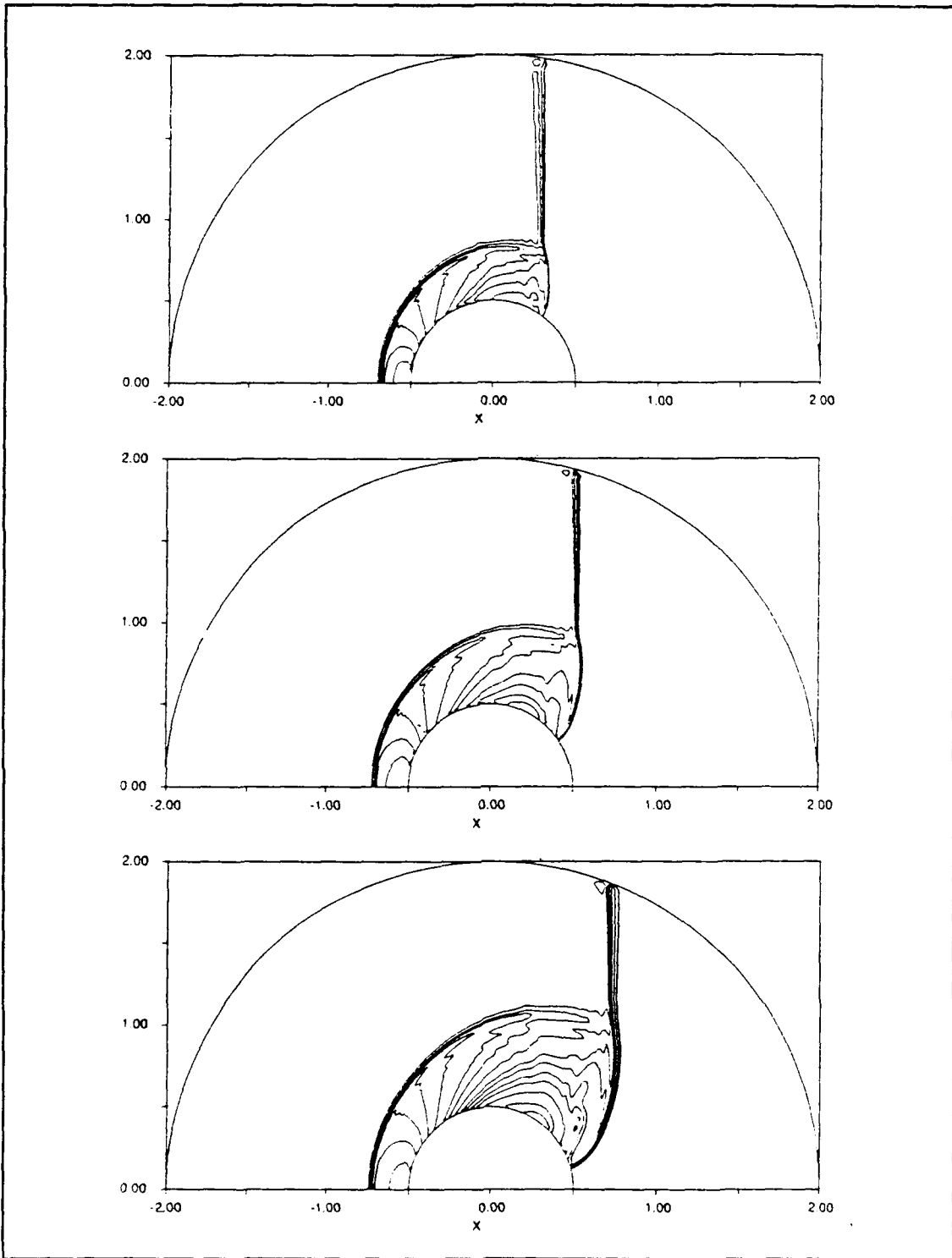


Figure 19. Density Contours, MacCormack Scheme,  
Time = d) 1.0642, e) 1.2690, and f) 1.4747

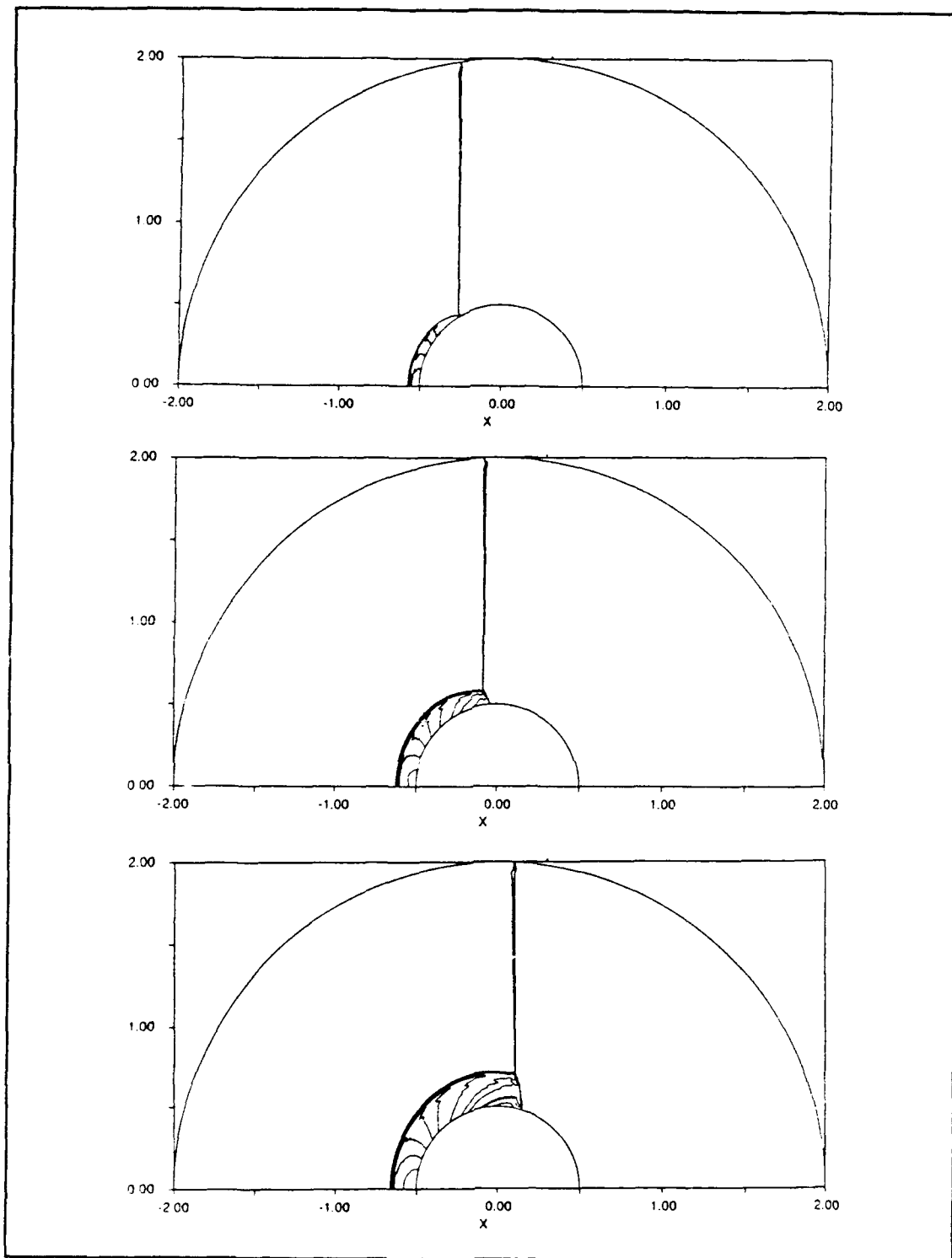


Figure 20. Pressure Contours, MacCormack Scheme,  
 Time = a) .4901, b) .6706, c) .8679

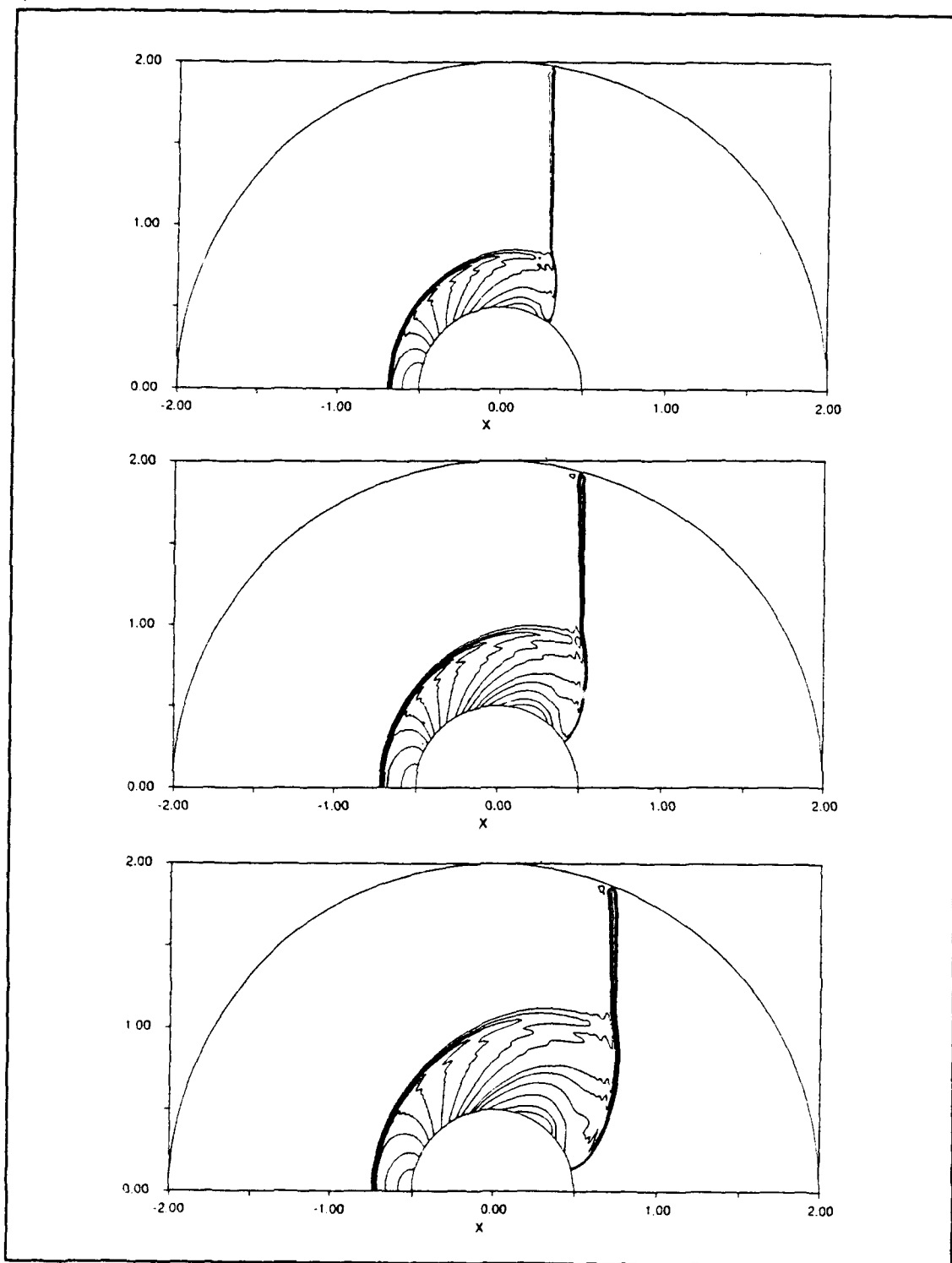


Figure 20. Pressure Contours, MacCormack Scheme,  
 Time = d) 1.0642, e) 1.2690, and f) 1.4747

The moment at which the incident shock and primary Mach stem pass over the top of the sphere is a critical time for the numerical simulations. The flow numerically overexpands and the pressure becomes negative in some instances. This problem has been reported for the numerical simulation of a two-dimensional flow about a triangular obstacle with a rounded top<sup>1</sup> using the MacCormack scheme. Variations of CFL number and smoothing coefficients for that case only delayed the onset of negative pressure. In this study, the MacCormack scheme was used with a CFL number of 0.5 and values for the smoothing coefficients of 3.0. Values of the smoothing coefficients of 2.0 did result in the flow numerically overexpanding just aft of the top of the sphere. The second-order TVD scheme used approximately the same operating parameters here as in the steady-state problem, i.e., CFL number of 0.5 and  $\delta_p = 3.0$ .

Figure 17c, density contours from the TVD scheme, shows the emergence of the primary slip surface just aft of the top of the sphere. In Figure 17c, the slip surface has rolled up into a vortex - not to be confused with the vortices that form downstream of spheres due to separation. Figure 19c, density contours for the MacCormack scheme at the same time instant, does not resolve the slip surface as distinctly as the TVD scheme. In the pressure contours for both schemes of Figures 18c and 20c, it is possible to see where the slip surface

impinges the body. At that point, a local pressure minimum occurs, and the pressure contours encircle it.

The density contours in the time intervals of Figures 17d to 17f for the TVD scheme show the emergence of the secondary slip surface. This is discernible as a "sinusoidally shaped" kink in the contours. This surface does not roll up into vortices like the primary slip surface does. The density contours of Figures 19d to 19f for the MacCormack scheme do not resolve the secondary slip surface.

Furthermore, during this same time, the secondary Mach stem rotates clockwise down to the body surface and propagates upstream within the reflected shock - body surface region. The pressure contours in Figures 18d to 18f for the TVD scheme and Figures 20d to 20f for the MacCormack scheme do not resolve this phenomena. Figure 21 is a plot of the surface pressure distributions which correspond to Figures 18d and 20d for the TVD and MacCormack schemes, respectively. The TVD scheme shows a small rise in the surface pressure at this secondary Mach stem, just ahead of the shock impingement point, at approximately 110 degrees from the front stagnation point. The MacCormack scheme shows a gradual rise in the surface pressure from this point to the shock impingement point. Note also in Figure 21, for the MacCormack scheme, the onset of pressure oscillations at the stagnation point similar to those when the MacCormack scheme was applied to the steady-

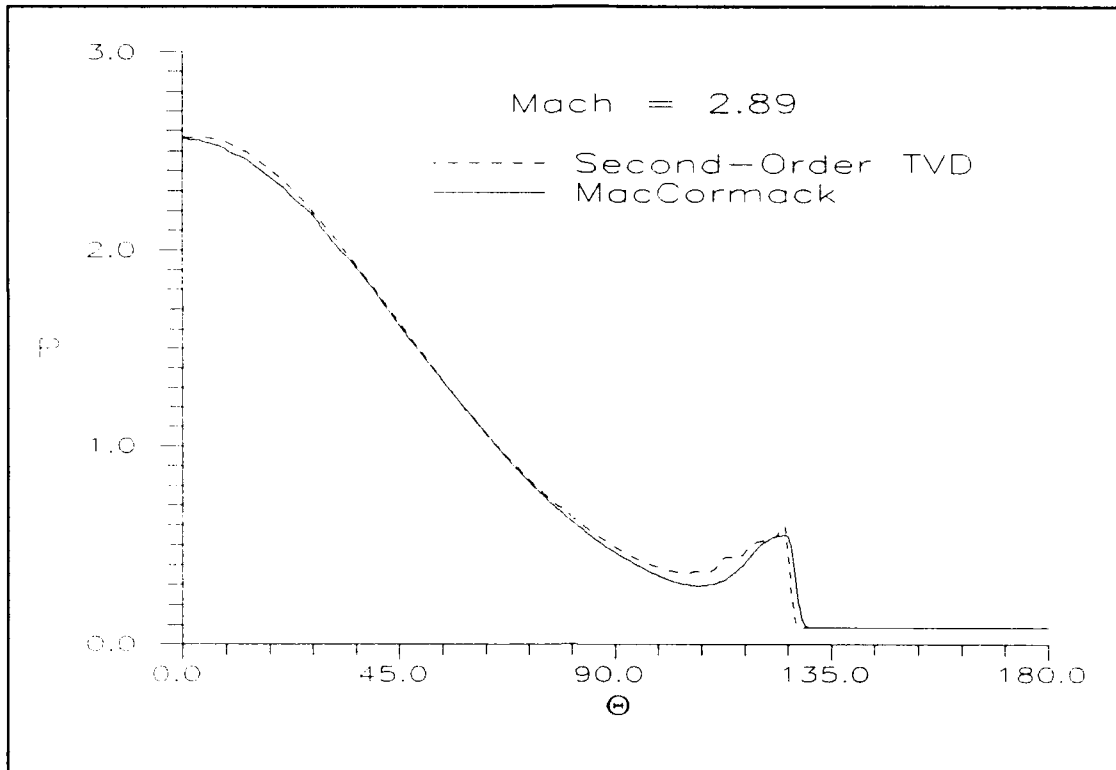


Figure 21. Surface Pressure Distribution, Second-Order TVD Scheme (Time = 1.0667) and MacCormack Scheme (Time = 1.0642)

state problem. These stagnation point oscillations also appear in the TVD scheme results as the shock impingement point moves further aft toward the rear stagnation point. Bennett et al<sup>32</sup> came upon this same phenomena for shock impingement on a cylinder using ARC2D - an inviscid, finite-difference scheme based on the Beam-Warming algorithm. Bennett et al extended the code to the Navier-Stokes equations and found that the pressure oscillations were removed. An interesting aside in the Bennett report was that the experimental data obtained by Pearson at the Ballistic Research Laboratory for the shock impingement on a cylinder

had "substantial high frequency oscillations." These oscillations were time-averaged for the final data set used in the comparisons to the inviscid and viscous ARC2D numerical predictions of pressure distributions.

A comparison of the effects of different limiters for the TVD scheme can be seen in the density contours of Figure 22. These were obtained at approximately the same time instant as those of Figure 18d using the limiter of Eq (46) for the linearly degenerate fields. This dissipative limiter barely resolves the primary slip surface and totally ignores the secondary slip surface. For this reason, the limiter of Eq (47) is recommended.

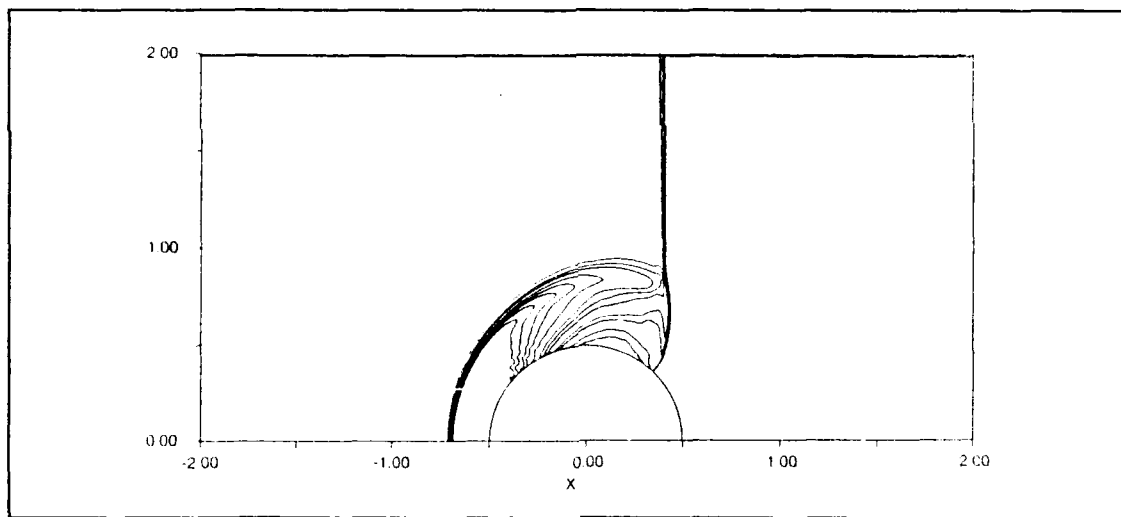


Figure 22. Density Contours, Second-Order TVD Scheme, Limiter of Eq (46), Time = 1.1546

A comparison between the results from the TVD scheme and Schlieren photographs from the Bryson and Gross<sup>22</sup> experiment are shown in the density contours in Figure 23 and 24. These

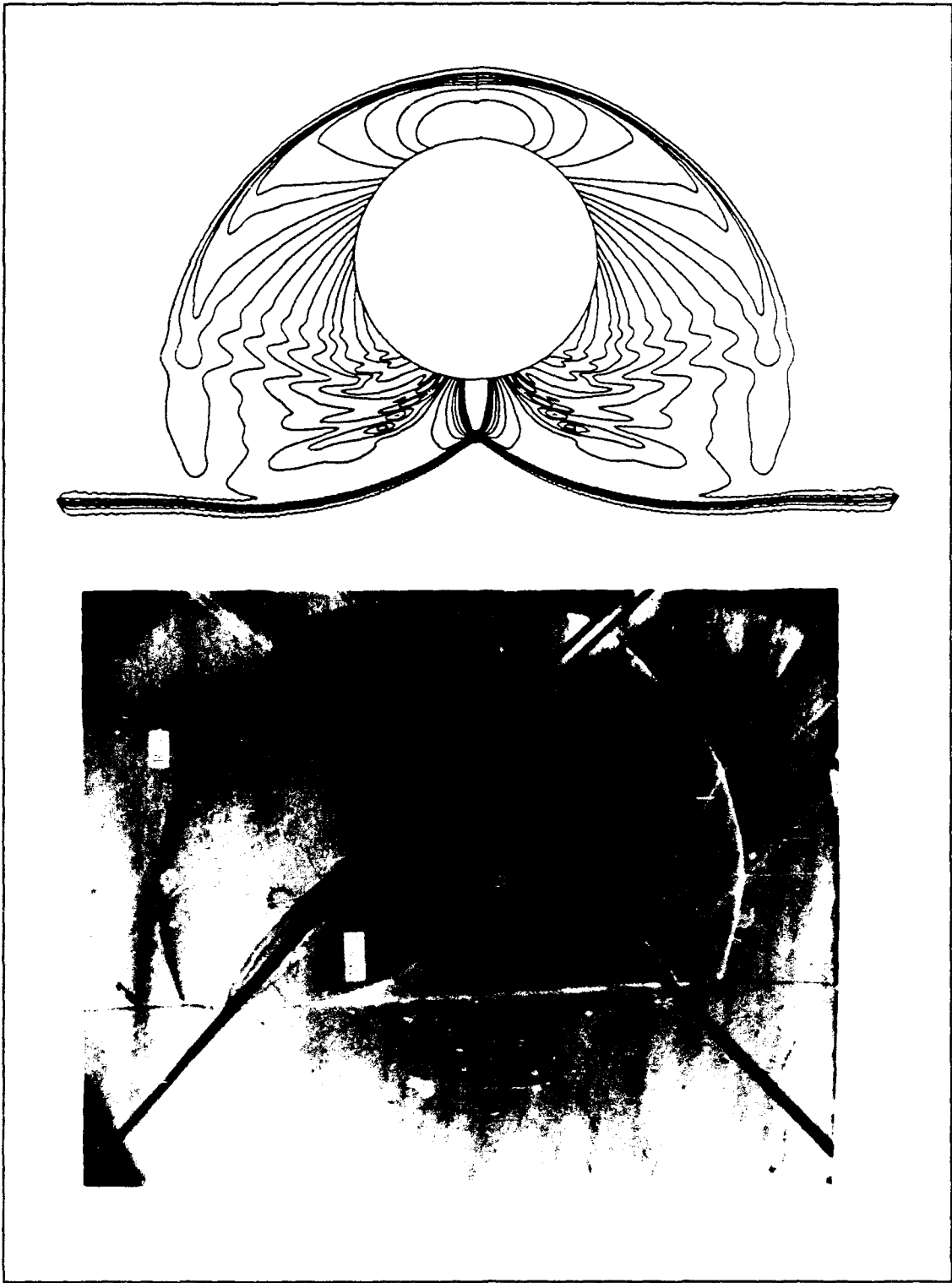


Figure 23. Density Contours, Second-Order TVD Scheme,  
Time = 1.7510,  $x = .9990$

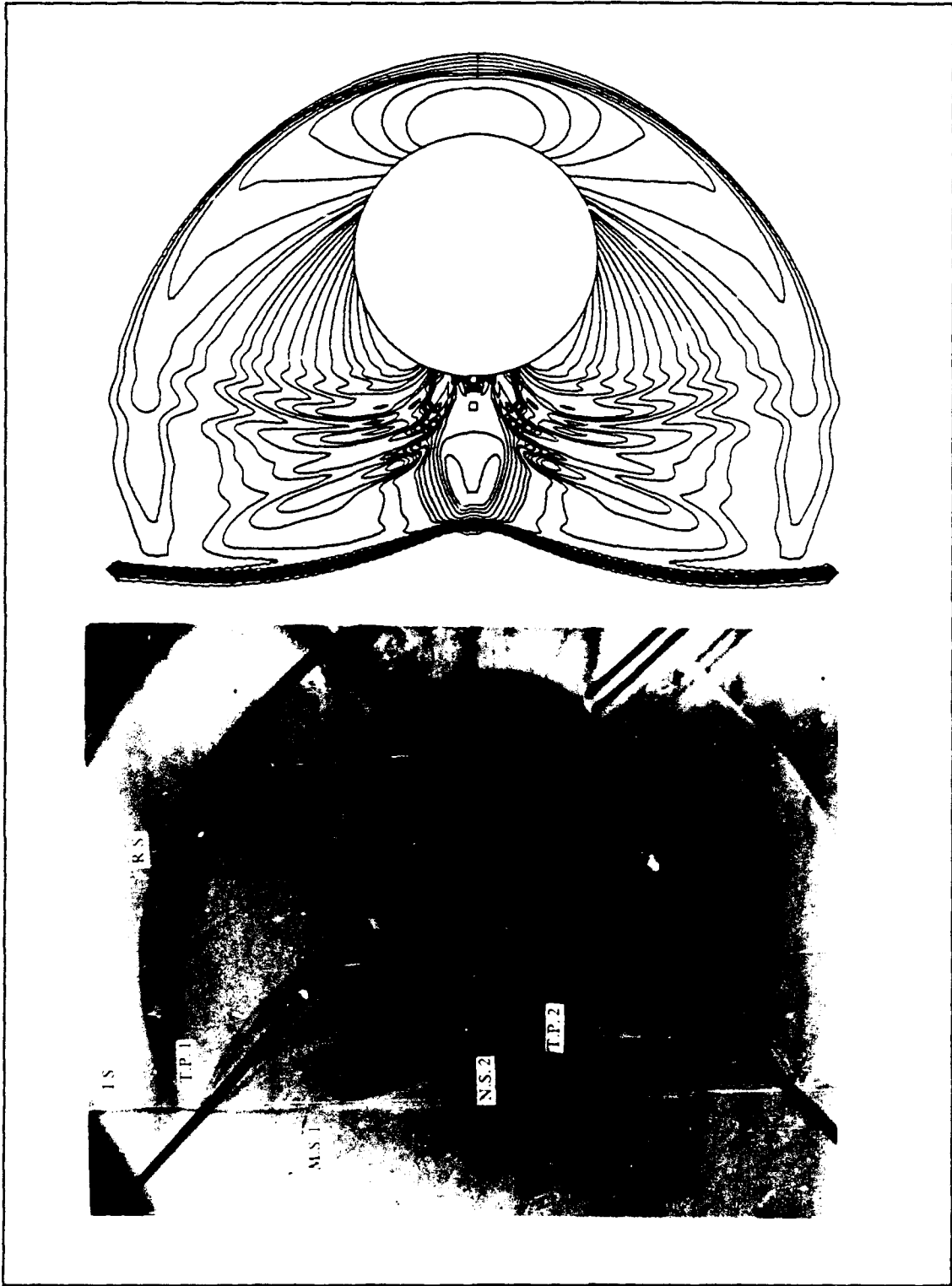


Figure 24. Density Contours, Second-Order TVD Scheme,  
Time = 2.0527,  $x = 1.3007$

correspond to incident shock locations of approximately 1 and 1.3 body diameters aft of the center of the sphere, respectively. The eight radial lines in the photos are nylon strings used to support the sphere in the test section. The triple points, slip surfaces, vortices, Mach stems, and reflected shocks are all favorably resolved by the TVD scheme when compared to the Schlieren photographs.

### 6.3 Comparison of Run Times and Time Step Count

A comparison of the run time for each time step and the number of steps required to reach the same selected times for the TVD and MacCormack schemes will be presented in this section.

A Stardent GS-2000 Graphics Supercomputer of the Aeronautics and Astronautics department of the Air Force Institute of Technology was used for this study. The numerical TVD scheme was optimized to allow for as much vectorization as possible. The MacCormack scheme has also been optimized. For the 251 x 101 grid, the computation times were approximately 4 seconds per time step and 2 seconds per time step for the TVD and MacCormack schemes, respectively. This corresponds to a data processing rate of  $1.58 \times 10^{-4}$  and  $7.89 \times 10^{-5}$  seconds per grid point per time step, respectively.

Table 3 compares the number of time steps, time, and percent time step increase for the TVD scheme and MacCormack schemes.

Table 3  
Comparison of Time Step Count and Time

TVD Scheme		MacCormack Scheme		% Count Rise
Count	Time	Count	Time	
200	.4924	258	.4901	29.0
300	.6727	386	.6706	28.7
400	.8703	517	.8679	29.3
500	1.0667	636	1.0642	27.2
600	1.2708	752	1.2690	25.3
700	1.4765	869	1.4747	24.1
800	1.6775	985	1.6751	23.1

For the same CFL number, the MacCormack scheme has a more restrictive time step size than the TVD scheme.

Finally, for the 251 x 101 grid, to reach a time of 1.6775, it takes approximately 35% longer with the TVD scheme than the MacCormack scheme. This is still under 1 hour and quite reasonable for a numerical simulation of this complexity.

## VII. Conclusions and Recommendations

An explicit, second-order accurate, finite-volume, TVD scheme has been developed for the Euler equations in axisymmetric form. A summary of conclusions from the results presented in this study and recommendations for further investigation are presented in the next two sections.

### 7.1 Conclusions

Numerical simulations of the steady-state, blunt-body problem were in excellent agreement with theory and experimental data over a wide range of Mach numbers in terms of shock standoff distance, bow-shock shape, and surface pressure distributions. The calculated entropy jump was also in excellent agreement with theory and experimental data. Comparisons with the MacCormack scheme show that the second-order TVD scheme better resolves the flowfield features and has a greater stability and robustness characteristic. It was shown that the choice of the entropy correction parameter,  $\delta_p$ , affects convergence rate and resolution of flowfield features.

Numerical simulations of the shock impingement problem with both schemes show that the TVD scheme's ability to resolve the complex, unsteady interactions during a blast-wave impact on a sphere are very good. Primary and secondary structures were resolved with the proper limiter for the

linearly degenerate fields. These flowfield structures were not resolved as well with the MacCormack scheme. For the TVD scheme, comparisons of flowfield structure to Schlieren photos from experiment were also very good.

These results suggest that the proposed TVD scheme can be a very useful tool in the efficient calculation of accurate solutions for the research, development and design of hypersonic blunt-body vehicles.

## 7.2 Recommendations

Recommendations for further study of the TVD scheme that are applicable to the steady-state blunt-body problem and the unsteady shock impingement problem are:

- 1) a systematic study of limiters and their effect on resolution of discontinuities,
- 2) extension to three-dimensional form using the axisymmetric form as a test bed,
- 3) incorporation of equilibrium and non-equilibrium effects, and
- 4) extension to the Navier-Stokes equations.

Difficulties anticipated with these recommendations include:

- 1) loss of time accuracy and
- 2) increased computer memory and CPU time requirements due to increased number of nodes and complexity of the governing equations.

Recommendations for further study of the steady-state problem blunt-body problem include:

- 1) automatic switching from a first-order to a second-order scheme for an impulsive start, or
- 2) gradual application of boundary conditions to allow an impulsive start, and
- 3) further analysis of the effects of the entropy correction function and parameter on convergence rate and resolution.

Recommendations for further study of the unsteady shock impingement problem include:

- 1) simulations for different structures - data from nuclear blast-wave effects are important for national security reasons<sup>33</sup>
- 2) analysis and investigation into the pressure oscillation phenomena (perhaps the Navier-Stokes equations will remove the phenomena as it did for Bennett et al<sup>32</sup>), and
- 3) development of better freestream boundary conditions to eliminate having to track the shock.

## Appendix: Nondimensionalization

The Euler equations of motion are nondimensionalized following the description by Beran in Reference 34. The freestream velocity,  $U_\infty$ , and the sphere radius,  $R_B$ , are the velocity and length scales, respectively. The freestream conditions are specified to be scales for the temperature and density. Consequently,

$$\begin{aligned}u &= u^*U_\infty & v &= v^*U_\infty \\x &= x^*R_B & y &= y^*R_B \\t &= t^*(R_B/U_\infty) \\T &= T^*T_\infty & \rho &= \rho^*\rho_\infty \\p &= p^*\rho_\infty U_\infty^2 & e &= e^*U_\infty^2\end{aligned}$$

The Mach number,  $M_\infty = U_\infty/c_\infty$ , where  $c_\infty$  is the freestream speed of sound, is used in the boundary conditions. A more convenient form of the Mach number is

$$M_\infty^2 = \frac{q_\infty^2}{c_\infty^2} = \frac{q_\infty^2}{\gamma RT_\infty}$$

where

$$q_\infty^2 = u_\infty^2 + v_\infty^2$$

The equation of state (perfect gas),  $p = \rho RT$ , is written in non-dimensional form as

$$p^* \rho_\infty U_\infty^2 = \rho^* \rho_\infty R T^* T_\infty$$

$$p^* U_\infty^2 = \rho^* T^* (R T_\infty) = \rho^* T^* \left( \frac{U_\infty^2}{\gamma M_\infty^2} \right)$$

$$p^* = \frac{\rho^* T^*}{\gamma M_\infty^2}$$

Note that in the freestream

$$p^* = (\gamma M_\infty^2)^{-1}$$

The pressure is eliminated in the equations of motion through another approach:

$$p = \rho R \frac{e}{c_v} = \rho (\gamma - 1) e$$

$$p^* = (\gamma - 1) \rho^* e^*$$

Note that in the freestream,

$$e^* = ((\gamma - 1) \gamma M_\infty^2)^{-1}$$

The definition of total energy leads to a reasonable scaling for  $E_t$ :

$$\begin{aligned} E_t &= \rho e + \frac{1}{2} \rho (u^2 + v^2) \\ E_t &= \rho_\infty U_\infty^2 (\rho^* e^* + \frac{1}{2} \rho^* ((u^*)^2 + (v^*)^2)) \\ E_t^* &= \rho^* e^* + \frac{1}{2} \rho^* ((u^*)^2 + (v^*)^2) \\ E_t &= E_t^* \rho^* U_\infty^2 \end{aligned}$$

Note that in the freestream,

$$E_t^* = \frac{1}{2} + ((\gamma - 1) \gamma M_\infty^2)^{-1}$$

The equations of motion in non-dimensional form turn out to be the same as the dimensional equations when the asterisks are dropped; the TVD schemes described need not be modified. The Mach number only enters into the problem through the specification of  $E_t$  in the far field.

## Bibliography

1. Yee, Helen C. A Class of High-Resolution Explicit and Implicit Shock-Capturing Methods. NASA Technical Memorandum 101088. Ames Research Center, Moffett Field CA, February 1989.
2. Trolinger, James D. et al. "Non-Intrusive Diagnostics for National Aerospace Plane Testing," AIAA 15th Aerodynamic Testing Conference. AIAA-88-2051. San Diego: American Institute of Aeronautics and Astronautics, May 1988.
3. Glaz, Harland M. "Numerical Computations in Gas Dynamics with High Resolution Schemes," Shock Tubes and Waves, Proceedings of the 16th International Symposium on Shock Tubes and Waves. Aachen, West Germany: VCH Verlagsgesellschaft, 1987.
4. Harten, Ami. "High Resolution Schemes for Hyperbolic Conservation Laws," Journal of Computational Physics, 49: 357-393 (1983).
5. Wang, J. C. T. and G. F. Widhopf. "A High-Resolution TVD Finite Volume Scheme for the Euler Equations in Conservation Form," AIAA 25th Aerospace Sciences Meeting. AIAA-87-0538. Reno: American Institute of Aeronautics and Astronautics, January 1987.
6. Shang, J. S. and Eswar Josyula. "Numerical Simulations of Non-Equilibrium Hypersonic Flow Past Blunt Bodies," AIAA 26th Aerospace Sciences Meeting. AIAA-88-0512. Reno: American Institute of Aeronautics and Astronautics, January 1988.
7. Anderson, John D., Jr. Modern Compressible Flow: With Historical Perspective. McGraw-Hill Series in Mechanical Engineering. New York: McGraw-Hill Book Company, 1982.
8. Anderson, Dale A. et al. Computational Fluid Mechanics and Heat Transfer. Series in Computational Methods in Mechanics and Thermal Sciences. New York: Hemisphere Publishing Corporation, 1984.
9. Richtmeyer, Robert D. and K. W. Morton. Difference Methods for Initial-Value Problems. Interscience Tracts in Pure and Applied Mathematics. New York: Interscience Publishers of John Wiley & Sons, 1967.

10. Anderson, John D., Jr. Hypersonic and High Temperature Gas Dynamics. McGraw-Hill Series in Aeronautical and Aerospace Engineering. New York: McGraw-Hill Book Company, 1989.
11. Roe, P.L. "Approximate Riemann Solvers, Parameter Vectors, and Difference Schemes," Journal of Computational Physics, 43: 357-372 (1981).
12. Thompson, Joe F. et al. Numerical Grid Generation, Foundations and Applications. New York: Elsevier Science Publishing Co., Inc., 1985.
13. Pulliam, Thomas H. and Joseph L. Steger. "Recent Improvements in Efficiency, Accuracy, and Convergence for Implicit Approximate Factorization Algorithms," AIAA 23rd Aerospace Sciences Meeting. AIAA-85-0360. Reno: American Institute of Aeronautics and Astronautics, January 1985.
14. Driver, Capt Mark A. and Capt Philip S. Beran. "Analysis of Transonic Turbine Rotor Cascade Flows Using a Finite-Volume Total Variation Diminishing (TVD) Scheme," AIAA/SAE/ASME/ASEE 26th Joint Propulsion Conference. AIAA-90-2127. Orlando: American Institute of Aeronautics and Astronautics, July 1990.
15. Roache, P. J. Computational Fluid Dynamics. Albuquerque: Hermosa Publishers, 1982.
16. Peyret, Roger and Thomas D. Taylor. Computational Methods for Fluid Flow. Springer-Verlag Series in Computational Physics. New York: Springer-Verlag, 1983.
17. Mounts, Jon S. et al. Program EAGLE User's Manual, Volume IV, Multi-Block, Implicit, Steady-State Euler Code. Technical Report AFATL-TR-88-11712. Air Force Armament Laboratory (AFATL), Armament Division (AFSC), Eglin AFB FL, September, 1988.
18. Young, Victor Y. C. and H. C. Yee. "Numerical Simulation of Shock Wave Diffraction by TVD Schemes," AIAA 25th Aerospace Sciences Meeting. AIAA-87-0112. Reno: American Institute of Aeronautics and Astronautics, January 1987.
19. Reshotko, Eli. Estimate of Shock Standoff Distance Ahead of a General Stagnation Point. NASA Technical Note D-1050. Lewis Research Center, Cleveland OH, August 1961.

20. Truitt, Robert Wesley. Hypersonic Aerodynamics. New York: The Ronald Press Company, 1959.
21. NACA Report 1135. Ames Aeronautical Laboratory, Moffett Field, CA
22. Bryson, A. E. and R. W. F. Gross. "Diffraction of Strong Shocks by Cones, Cylinders, and Spheres," Journal of Fluid Mechanics, 10: 1-22 (Feb-June 1961).
23. Heilig, W. "The Influence of Wall and Shock Curvature on Shock Reflection Processes," Shock Tubes and Waves, Proceedings of the 16th International Symposium on Shock Tubes and Waves. Aachen, West Germany: VCH Verlagsgesellschaft, 1987.
24. Yee, H. C. and P. Kutler. Application of Second-Order Accurate Total Variation Diminishing (TVD) Schemes to the Euler Equations in General Geometries. NASA Technical Memorandum 85845. Ames Research Center, Moffett Field, CA, August 1983.
25. Takayama, Kazuyoshi. "Holographic Interferometric Study of Shock Wave Propagation in Two-Phase Media," Shock Tubes and Waves, Proceedings of the 16th International Symposium on Shock Tubes and Waves. Aachen, West Germany: VCH Verlagsgesellschaft, 1987.
26. Baer, A. L. Pressure Distributions on a Hemisphere Cylinder at Supersonic and Hypersonic Mach Numbers. Technical Note AEDC-TN-61-96. Von Karman Gas Dynamics Facility (VKF), Arnold Engineering and Development Center (AFSC), Arnold AFB TN, August 1961.
27. Hindman, Richard G. "Generalized Coordinate Forms of Governing Fluid Equations and Associated Geometrically Induced Errors," AIAA Journal, 20: 1359-1367 (October 1982).
28. Yee, Helen C. et al. "Implicit Total Variation Diminishing (TVD) Schemes for Steady-State Calculations," Journal of Computational Physics, 57: 327-360 (1985).
29. Saida, N. et al. "Unsteady Shock Boundary Layer Interaction Ahead of a Forward Facing Step," Shock Tubes and Waves, Proceedings of the 16th International Symposium on Shock Tubes and Waves. Aachen, West Germany: VCH Verlagsgesellschaft, 1987.

30. Harten, Ami et al. "On Finite-Difference Approximations and Entropy Conditions for Shocks," Communications on Pure and Applied Mathematics, XXIX: 297-322 (1976).
31. Rizzi, Arthur. "Spurious Entropy Production and Very Accurate Solutions to the Euler Equations," AIAA 17th Fluid Dynamics, Plasmadynamics, and Lasers Conference. AIAA-84-1644. Snowmass CO: American Institute of Aeronautics and Astronautics, June 1984.
32. Bennett, B. C. et al. "Viscous Effects on Blast Wave Flowfields," AIAA 24th Aerospace Sciences Meeting. AIAA-86-0031. Reno: American Institute of Aeronautics and Astronautics, January 1986.
33. Kutler, P. and A. R. Fernquist. Computations of Blast-Wave Encounter with Military Targets. Flow Simulations, Inc. Report No. 80-02, April 30, 1980.
34. Beran, Capt Philip S. Class notes in AERO 752, Computational Aerodynamics. School of Engineering, Air Force Institute of Technology (AU), Wright-Patterson AFB OH, March - May 1990.

## Vita

Monty Hughson was born on July 9, 1957 in Manistique, Michigan. He attended William J. Palmer High School in Colorado Springs, Colorado and graduated in June of 1975. He enlisted in the Air Force in February of 1976 and served 9 years as a Disbursement Accounting Specialist at Lowry AFB CO and Yokota AB Japan. Monty was selected for the Airman Education and Commissioning Program (AECM) and attended the University of Texas at Austin where he obtained his Bachelor of Science Degree in Aerospace Engineering in December of 1984. His next assignment was at the Air Force Armament Laboratory (AFATL) at Eglin AFB FL, where he analyzed missile and projectile aerodynamics using computational fluid dynamics and experimentation. After four years at AFATL he attended the Air Force Institute of Technology at Wright-Patterson AFB OH to complete a Master of Science degree in Aeronautical Engineering.

Current Address: 1000 Middy Drive  
Wright-Patterson AFB, OH 45433  
(513) 252-3831

Permanent Address: 4665 S. Splendid Circle  
Colorado Springs, Colorado 80917  
(719) 597-2571

REPORT DOCUMENTATION PAGE			Form Approved OMB No. 0704-0188		
<small>Instructions: This form is to be filled out by the author(s) and submitted to the reporting agency. It is not to be filled out by the agency. The form is to be filled out by the author(s) and submitted to the reporting agency. It is not to be filled out by the agency. The form is to be filled out by the author(s) and submitted to the reporting agency. It is not to be filled out by the agency.</small>					
1. AGENCY USE ONLY (Leave blank)		2. REPORT DATE December 1990	3. REPORT TYPE AND DATES COVERED Master's Thesis		
4. TITLE AND SUBTITLE ANALYSIS OF BLUNT-BODY FLOWS USING A TOTAL VARIATION DIMINISHING (TVD) SCHEME AND THE MACCORMACK SCHEME			5. FUNDING NUMBERS		
6. AUTHOR(S)  Montgomery C. Hughson, Capt, USAF			7. PERFORMING ORGANIZATION REPORT NUMBER  AFIT/GAE/ENY/90D-10		
8. PERFORMING ORGANIZATION NAME(S) AND ADDRESS(ES)  Air Force Institute of Technology WPAFB OH 45433-6583			10. SPONSORING / MONITORING AGENCY REPORT NUMBER		
9. SPONSORING / MONITORING AGENCY NAME(S) AND ADDRESS(ES)  Dr Joseph Shang WRDC/FIMME WPAFB, OH 45433					
11. SUPPLEMENTARY NOTES					
12a. DISTRIBUTION AVAILABILITY STATEMENT  Approved for public release; distribution unlimited			12b. DISTRIBUTION CODE		
13. ABSTRACT (Maximum 200 words) An explicit second-order accurate, total variation diminishing (TVD) scheme and the MacCormack scheme are applied to the Euler equations in axisymmetric form to study hypersonic blunt-body flows. The modified flux approach of Harten, with modification by Yee, for two-dimensional flows is extended to treat axisymmetric flows. Calculated flow properties for the steady-state, blunt-body problem such as shock standoff distance, bow shock shape, surface pressure distribution and entropy jump conditions are compared to theory, results from the MacCormack scheme, and experimental data for Mach numbers of 3.0, 4.03, 5.06, 6.03 and 8.1. Additionally, the TVD and MacCormack schemes are used to simulate numerically the unsteady shock impingement on a sphere. Results are compared to experimental data for a shock Mach number of 2.89. Analysis of the numerical simulations provide suitable ranges of values for the entropy correction parameter and the Courant (CFL) number. The high-resolution and robustness of the TVD scheme is clearly shown. <i>Keywords:</i>					
14. SUBJECT TERMS  Numerical Methods, Computational Fluid Dynamics TVD-Schemes, Axisymmetric Flow, Finite-Volume Method.			15. NUMBER OF PAGES 95		
			16. PRICE CODE (74D)		
17. SECURITY CLASSIFICATION OF REPORT Unclassified	18. SECURITY CLASSIFICATION OF THIS PAGE Unclassified	19. SECURITY CLASSIFICATION OF ABSTRACT Unclassified	20. LIMITATION OF ABSTRACT UL		

## GENERAL INSTRUCTIONS FOR COMPLETING SF 298

The Report Documentation Page (RDP) is used in announcing and cataloging reports. It is important that this information be consistent with the rest of the report, particularly the cover and title page. Instructions for filling in each block of the form follow. It is important to **stay within the lines to meet optical scanning requirements.**

### **Block 1. Agency Use Only (Leave Blank)**

**Block 2. Report Date.** Full publication date including day, month, and year, if available (e.g. 1 Jan 88). Must cite at least the year.

**Block 3. Type of Report and Dates Covered.** State whether report is interim, final, etc. If applicable, enter inclusive report dates (e.g. 10 Jun 87 - 30 Jun 88).

**Block 4. Title and Subtitle.** A title is taken from the part of the report that provides the most meaningful and complete information. When a report is prepared in more than one volume, repeat the primary title, add volume number, and include subtitle for the specific volume. On classified documents enter the title classification in parentheses.

**Block 5. Funding Numbers.** To include contract and grant numbers; may include program element number(s), project number(s), task number(s), and work unit number(s). Use the following labels:

<b>C</b> - Contract	<b>PR</b> - Project
<b>G</b> - Grant	<b>TA</b> - Task
<b>PE</b> - Program Element	<b>WU</b> - Work Unit Accession No.

**Block 6. Author(s).** Name(s) of person(s) responsible for writing the report, performing the research, or credited with the content of the report. If editor or compiler, this should follow the name(s).

**Block 7. Performing Organization Name(s) and Address(es).** Self-explanatory.

**Block 8. Performing Organization Report Number.** Enter the unique alphanumeric report number(s) assigned by the organization performing the report.

**Block 9. Sponsoring/Monitoring Agency Names(s) and Address(es).** Self-explanatory.

**Block 10. Sponsoring/Monitoring Agency Report Number.** (If known)

**Block 11. Supplementary Notes.** Enter information not included elsewhere such as: Prepared in cooperation with...; Trans. of ..., To be published in .... When a report is revised, include a statement whether the new report supersedes or supplements the older report.

### **Block 12a. Distribution/Availability Statement.**

Denote public availability or limitation. Cite any availability to the public. Enter additional limitations or special markings in all capitals (e.g. NOFORN, REL, ITAR)

**DOD** - See DoDD 5230.24, "Distribution Statements on Technical Documents."

**DOE** - See authorities

**NASA** - See Handbook NHB 2200.2.

**NTIS** - Leave blank.

### **Block 12b. Distribution Code.**

**DOD** - DOD - Leave blank

**DOE** - DOE - Enter DOE distribution categories from the Standard Distribution for Unclassified Scientific and Technical Reports

**NASA** - NASA - Leave blank

**NTIS** - NTIS - Leave blank.

**Block 13. Abstract.** Include a brief (Maximum 200 words) factual summary of the most significant information contained in the report.

**Block 14. Subject Terms.** Keywords or phrases identifying major subjects in the report.

**Block 15. Number of Pages.** Enter the total number of pages.

**Block 16. Price Code.** Enter appropriate price code (NTIS only).

**Blocks 17. - 19. Security Classifications.** Self-explanatory. Enter U.S. Security Classification in accordance with U.S. Security Regulations (i.e., UNCLASSIFIED). If form contains classified information, stamp classification on the top and bottom of the page.

**Block 20. Limitation of Abstract.** This block must be completed to assign a limitation to the abstract. Enter either UL (unlimited) or SAR (same as report). An entry in this block is necessary if the abstract is to be limited. If blank, the abstract is assumed to be unlimited.